Earth matter effects at very long baselines and the neutrino mass hierarchy

Raj Gandhi,[1,*] Pomita Ghoshal,[1,†] Srubabati Goswami,[1,2,‡] Poonam Mehta,[1,3,§] and S. Uma Sankar[4,‖]

[1]*Harish-Chandra Research Institute, Chhatnag Road, Jhunsi, Allahabad 211 019, India*
[2]*Technische Universität München, James-Franck-Strasse, D-85748 Garching, Germany*
[3]*Department of Particle Physics, Weizmann Institute of Science, Rehovot 76 100, Israel*
[4]*Department of Physics, Indian Institute of Technology, Powai, Mumbai 400 076, India*

(Received 13 March 2005; revised manuscript received 5 August 2005; published 1 March 2006)

We study matter effects which arise in the muon neutrino oscillation and survival probabilities relevant to atmospheric neutrino and very long baseline (>4000 Km) beam experiments. The interrelations between the three probabilities $P_{\mu e}$, $P_{\mu\tau}$, and $P_{\mu\mu}$ are examined. It is shown that large and observable sensitivity to the neutrino mass hierarchy can be present in $P_{\mu\mu}$ and $P_{\mu\tau}$. We emphasize that at baselines >7000 Km, matter effects in $P_{\mu\tau}$ are important under certain conditions and can be large. The muon survival rates in experiments with very long baselines thus depend on matter effects in both $P_{\mu\tau}$ and $P_{\mu e}$. We also indicate where these effects provide sensitivity to θ_{13} and identify ranges of energies and baselines where this sensitivity is maximum. The effect of parameter degeneracies in the three probabilities at these baselines and energies is studied in detail and large parts of the parameter space are identified which are free from these degeneracies. In the second part of the paper, we focus on using the matter effects studied in the first part as a means of determining the mass hierarchy via atmospheric neutrinos. Realistic event rate calculations are performed for a charge discriminating 100 kT iron calorimeter which demonstrate the possibility of realizing this very important goal in neutrino physics. It is shown that for atmospheric neutrinos, a careful selection of energy and baseline ranges is necessary in order to obtain a statistically significant signal, and that the effects are largest in bins where matter effects in both $P_{\mu e}$ and $P_{\mu\tau}$ combine constructively. Under these conditions, up to a 4σ signal for matter effects is possible (for $\Delta_{31} > 0$) within a time scale appreciably shorter than the one anticipated for neutrino factories.

DOI: 10.1103/PhysRevD.73.053001 PACS numbers: 14.60.Pq, 13.15.+g, 14.60.Lm

I. INTRODUCTION

It is fair to say that over the last few years there has been a qualitative shift in the nature of the goals to be pursued in neutrino physics. This has been the result of steadily accumulating evidence in favor of nonzero neutrino mass and flavor oscillations. Results from atmospheric neutrino experiments [1–7], corroborated by the accelerator beam based *KEK to Kamioka (K2K)* experiment [8] have provided firm evidence for $\nu_\mu \to \nu_\tau$ oscillations with maximal (or almost maximal) mixing. The solar neutrino results [9–16], when combined with the results of the reactor based *KamLAND* experiment [17], have established the LMA-MSW solution [18] as the most favored explanation for the solar neutrino deficit. For recent global analyses of solar, reactor, accelerator, and atmospheric data, see [19–22]. In Table I, we summarize the best-fit values and 3σ intervals of allowed values of important oscillation parameters gleaned from experiments so far obtained from global three flavor neutrino analysis [19,21].

The shift has been from a search for understanding the particle physics and/or the astrophysics driving the solar and atmospheric neutrino deficits to one where we seek to make increasingly precise measurements of neutrino mass and mixing matrix parameters. Experiments planned to yield results over the next 10 to 15 years thus reflect this change of emphasis. A significant number of the planned projects are long baseline[1] endeavours using either (a) *a conventional proton beam* colliding with a target to produce pions which then decay to give muon neutrinos, or (b) *superbeams*, which are essentially technologically upgraded versions of present conventional beams, or, finally, (c) *reactor sources* with both near and far detectors for reduced systematic errors.

To begin with, we enumerate and briefly describe the planned projects in the three categories above which are expected to give results over the next decade or decade and a half. For a recent detailed study of their capabilities we refer the reader to [23] and references therein.

(i) *Conventional* beam experiments will have as their primary goal the improvement in the precision of the atmospheric oscillation parameters, Δ_{31} and

*Electronic address: raj@mri.ernet.in
†Electronic address: pomita@mri.ernet.in
‡Electronic address: sruba@mri.ernet.in,sruba@ph.tum.de
§Electronic address: mpoonam@mri.ernet.in, poonam.mehta@weizmann.ac.il
‖Electronic address: uma@phy.iitb.ac.in

[1]By "long baseline" we actually mean the L/E range of about 50–500 Km/GeV. For accelerator experiments, this translates to baselines conventionally termed "long," but for the lower reactor neutrino energies, the baselines are actually 1–2 Km.

TABLE I. Best-fit values and 3σ intervals for three flavor neutrino oscillation parameters from global data including solar, atmospheric, reactor (KamLAND and CHOOZ), and accelerator (K2K) experiments [19,21]. Here $\Delta_{ij} \equiv m_i^2 - m_j^2$.

Parameter	Best-fit value	3σ allowed range
$\Delta_{21}[10^{-5}\text{eV}^2]$	8.3	7.2–9.1
$\Delta_{31}[10^{-3}\text{eV}^2]$	2.2	1.4–3.3
$\sin^2\theta_{12}$	0.30	0.23–0.38
$\sin^2\theta_{23}$	0.50	0.34–0.68
$\sin^2\theta_{13}$	0.00	≤ 0.047

$\sin^2 2\theta_{23}$. The *Main Injector Neutrino Oscillation Search (MINOS)* project [24], located in the U.S., with a baseline from Fermilab to Soudan mine in the U.S. state of Minnesota (735 Km), will utilize a 5.4 kT magnetized iron calorimeter and initially an $\langle E_\nu \rangle \simeq 3$ GeV to primarily measure muon survival events. By measuring the absolute event rate and the energy distribution for muons produced via charged current (CC) scattering, Δ_{31} may be determined to within about 10% to 20% of the current best-fit value. In addition, by measurements in the electron appearance channel, MINOS may provide a possibly improved upper bound on $\sin^2 2\theta_{13}$, by a factor of 1.5 to 2. In Europe, the two experiments planned in this category are the *Imaging Cosmic And Rare Underground Signals (ICARUS)* project [25], a 2.35 kT liquid Argon detector, and the *Oscillation Project with Emulsion-tRacking Apparatus (OPERA)* [26], a 1.65 kT emulsion cloud chamber which will ride the 732 Km CERN to Gran Sasso baseline and will be powered by the CNGS beam. The beam energy is higher, resulting in neutrinos which are kinematically capable of producing τ leptons ($\langle E_\nu \rangle \simeq 17$ GeV). In addition, these detectors can identify muons and electrons. It is thus anticipated that in addition to an improved precision in Δ_{31}, an improvement in the current bound on $\sin^2 2\theta_{13}$ may be possible at the same levels as anticipated with MINOS.

(ii) *Superbeam* experiments utilize the same basic principle used in conventional beam experiments but incorporate substantial technological improvements. This includes higher power beams and the idea of an ''off-axis'' location for the detector. One of the planned projects is the 295 Km *Tokai to Kamioka (T2K)* project [27], with *Super-Kamiokande (SK)* as the far detector of total mass 50 kT and $\langle E_\nu \rangle \simeq 0.76$ GeV. Similarly, the *NuMI Off-Axis ν_e Appearance experiment* (NOνA) [28] is planned for location in the U.S., with a probable 812 Km baseline terminating in a 30 kT calorimeter and $\langle E_\nu \rangle \simeq 2.2$ GeV. Both experiments primarily aim at heightened sensitivity to $\sin^2 2\theta_{13}$ via the electron appearance channel. It is anticipated that the upper bound on this parameter will be improved by a factor of 4 over a 5-year running period.
As discussed in [23], the combination of conventional and superbeam experiments over the next 10–12 years will improve the precision on Δ_{31} by an order of magnitude, while the improvement in $\sin^2 2\theta_{23}$ will be much more modest, i.e. by a factor of about 2.

(iii) Planned experiments in the *reactor* category [29] include *KASKA* in Japan [30], one in Diablo Canyon, USA [31] and another in Daya Bay, China [31], and an upgraded version of *CHOOZ* [32], called *Double-CHOOZ* [33] in France. Reactor experiments detect the electron antineutrino flux by the inverse beta-decay process and focus on improved measurements of $\sin^2 2\theta_{13}$, using a near detector to lower systematics. A factor of 6 improvement in the present upper bound on this parameter is expected.

To summarize, the above experiments will, over the next 10–12 years, greatly improve the precision on Δ_{31}, affect a very modest improvement in the existing measurements for $\sin^2 2\theta_{23}$, and improve the upper bound on $\sin^2 2\theta_{13}$ by a factor of 2 to 6, depending on the experiment. We note that given their insensitivity to matter effects,[2] they will not be able to conclusively determine the sign of Δ_{31} and thus will not establish whether neutrino masses follow a normal hierarchy or an inverted one.[3] This may thus leave one of the major questions of neutrino physics unresolved over the time scale considered here (10–12 years). Besides requiring a baseline long enough to allow matter oscillations to develop, the resolution of this issue, in general, requires a detector which can distinguish the sign of the lepton produced in a CC interaction. Over a longer term, progress in this direction may be possible via the proposed megaton water Cerenkov detectors [34]. Even though they do not have the capability to distinguish the charge on an event by event basis, once enough statistics are collected (≈ 2 megaton year exposures), it may be possible to use the differences in total and differential CC cross sections between neutrinos and antineutrinos to obtain a statistical determination of the sign of Δ_{31} [35–37]. Additionally, if neutrino factories are built, they will be able to resolve this question in a definitive fashion [38]. This paper examines the possibility of resolving this issue using atmospheric muon neutrinos over the same time frame as the long

[2]All baselines for the listed experiments are around or below 800 Km.

[3]Combined results from T2K [27] and the NuMI Off-Axis [28] experiment may be able to infer the neutrino mass hierarchy. However, first results on this would be available about 6 years after the NOνA far detector is completed, i.e., around 2017. In addition, inferring the hierarchy may be complicated by ambiguities resulting from uncertainties in $\sin^2 2\theta_{13}$ and δ_{CP}.

baseline program described above (shorter compared to the time scale of neutrino factories).

In the first part of this paper, we study the physics related to the sensitivity of the muon neutrino survival probability to matter. In general, $P_{\mu\mu} = 1 - P_{\mu e} - P_{\mu\tau}$, and one normally assumes that the dependence of $P_{\mu\mu}$ on matter effects arises primarily from its $P_{\mu e}$ component while matter effects in $P_{\mu\tau}$ remain small. This is because ν_μ and ν_τ have the same coherent interactions with the Earth's matter. In [39] recently, it was shown that contrary to expectations, the $\nu_\mu \to \nu_\tau$ oscillation probability $P_{\mu\tau}$ *can also undergo significant change* (for instance, a reduction as high as $\sim$70% or an increase of $\sim$15%) *at very long baselines* ($>$ 6000 Km) over a broad band of atmospheric (GeV) neutrino energies *due to matter effects*. Given the fact that the atmospheric neutrino flux is a sharply falling function of energy in the few GeV range ($\frac{dN_\nu}{dE} \propto E^{-3.6}$) and that the production of τ leptons via CC is kinematically suppressed here, a direct observation of this effect via appearance in an atmospheric neutrino experiment may be difficult. However, large matter effects in $P_{\mu\tau}$ can cause correspondingly large changes in $P_{\mu\mu}$, and we explore the consequences of this in our paper. In particular, in the next section, we systematically discuss the interrelation between the three probabilities $P_{\mu e}$, $P_{\mu\mu}$, and $P_{\mu\tau}$ and study the ranges of energies and path lengths where they combine in a synergistic manner to give large effects. We also examine the problem of parameter degeneracies in these oscillation probabilities with reference to very long baselines.

The remaining part of the paper studies observational consequences of these effects for muon survival rates with particular emphasis on resolving the hierarchy issue in an atmospheric neutrino setting, using a detector capable of lepton charge discrimination. Earlier studies of this were undertaken in [40–42] and, more recently, in [43–45]. We also note that the muon survival rate is a major constituent of the signal in the existing SK [2,3] detector, the planned megaton water Cerenkov detectors like *Underground Nucleon decay and Neutrino Observatory (UNO)* or *Hyper-Kamiokande* [27,34,46], and several detectors considered for future long baseline facilities [47], for which the discussion below may be of relevance.

II. DISCUSSION OF THE MATTER PROBABILITIES: $P^m_{\mu e}$, $P^m_{\mu\tau}$, AND $P^m_{\mu\mu}$

Analytical expressions for oscillation probabilities for neutrino propagation in vacuum and Earth's matter have been extensively studied in the literature [48–64]. The neutrino flavor states are linear superpositions of the mass eigenstates with well-defined masses:

$$|\nu_\alpha\rangle = \sum_i U_{\alpha i}|\nu_i\rangle, \tag{1}$$

where U is a 3×3 unitary matrix known as the Pontecorvo-Maki-Nakagawa-Sakata mixing matrix. We use the standard parametrization of U in terms of three mixing angles and a Dirac-type phase (ignoring Majorana phases), viz.,

$$U = \begin{pmatrix} c_{12}c_{13} & s_{12}c_{13} & s_{13}e^{-i\delta_{CP}} \\ -c_{23}s_{12} - s_{23}s_{13}c_{12}e^{i\delta_{CP}} & c_{23}c_{12} - s_{23}s_{13}s_{12}e^{i\delta_{CP}} & s_{23}c_{13} \\ s_{23}s_{12} - c_{23}s_{13}c_{12}e^{i\delta_{CP}} & -s_{23}c_{12} - c_{23}s_{13}s_{12}e^{i\delta_{CP}} & c_{23}c_{13} \end{pmatrix}, \tag{2}$$

where $c_{ij} \equiv \cos\theta_{ij}$, $s_{ij} \equiv \sin\theta_{ij}$, and δ_{CP} is the *CP*-violating phase.

For the purpose of our discussion in the first three subsections here, besides the approximation of constant density, we set $\Delta_{21} \equiv \Delta_{sol} = 0$. Consequently the mixing angle θ_{12} and the *CP* phase δ_{CP} drop out of the oscillation probabilities. This approximation simplifies the analytical expressions and facilitates the qualitative discussion of matter effects. We have checked that this works well (up to a few percent) at the energies and length scales relevant here. However, all the plots we give in this paper are obtained by numerically solving the full three flavor neutrino propagation equation assuming the Preliminary Reference Earth Model (PREM) [65] density profile for the earth. We use $\Delta_{31} = 0.002$ eV^2 and $\sin^2 2\theta_{23} = 1$ unless otherwise mentioned. Further, the numerical calculations assume $\Delta_{21} = 8.3 \times 10^{-5}$ eV^2, $\sin^2\theta_{12} = 0.27$ [17], and $\delta_{CP} = 0$. The effect of varying the *CP* phase over the entire range (0 to 2π) will be taken up in Subsection II D), where we include analytic expressions which take into account small subleading effects and discuss the associated parameter degeneracies.

A. Review of $P_{\mu e}$ in matter

We first review $\nu_\mu \to \nu_e$ oscillations in matter. In vacuum, the $\nu_\mu \to \nu_e$ oscillation probability is

$$P^{v}_{\mu e} = \sin^2\theta_{23}\sin^2 2\theta_{13}\sin^2(1.27\Delta_{31}L/E), \tag{3}$$

where $\Delta_{31} \equiv m^2_3 - m^2_1$ is expressed in eV^2, L in Km, and E in GeV. In the constant density approximation, matter effects can be taken into account by replacing Δ_{31} and θ_{13} in Eq. (3) by their matter dependent values, i.e.,

$$P^{m}_{\mu e} = \sin^2\theta_{23}\sin^2 2\theta^m_{13}\sin^2(1.27\Delta^m_{31}L/E). \tag{4}$$

Here Δ^m_{31} and $\sin 2\theta^m_{13}$ are given by

$$\Delta^{m}_{31} = \sqrt{(\Delta_{31}\cos 2\theta_{13} - A)^2 + (\Delta_{31}\sin 2\theta_{13})^2},$$
$$\sin 2\theta^{m}_{13} = \sin 2\theta_{13}\frac{\Delta_{31}}{\Delta^{m}_{31}}, \quad (5)$$

where,

$$A = 2\sqrt{2}\,G_F\,n_e\,E = 0.76\times 10^{-4}\rho(\mathrm{gm/cc})\,E(\mathrm{GeV}).$$

The resonance condition[4] is $A = \Delta_{31}\cos 2\theta_{13}$, which gives

$$E_{res} = \frac{\Delta_{31}\cos 2\theta_{13}}{2\sqrt{2}G_F n_e}. \quad (6)$$

Naively, one would expect $P^{m}_{\mu e}$ to be maximum at $E = E_{res}$ since $\sin 2\theta^{m}_{13} = 1$. But this is not true in general because at this energy Δ^{m}_{31} takes its minimum value of $\Delta_{31}\sin 2\theta_{13}$ and $P^{m}_{\mu e}$ remains small for path lengths of $L \leq 1000$ Km. If L is chosen suitably large so as to satisfy $(1.27\Delta_{31}\sin 2\theta_{13}L/E) \geq \pi/4$, then $P^{m}_{\mu e}$ can attain values ≥ 0.25 for $\sin^2 2\theta_{23} = 1$. For $\Delta_{31} = 0.002$ eV^2 and $\sin^2 2\theta_{13} = 0.1$, one needs $L \geq 6000$ Km to satisfy the above condition.

In particular, $P^{m}_{\mu e}$ is maximum when both

$$\sin 2\theta^{m}_{13} = 1$$

and

$$\sin^2(1.27\Delta^{m}_{31}L/E) = 1 \quad \text{or,}$$
$$(1.27\Delta^{m}_{31}L/E) = [(2p+1)\pi/2]$$

are satisfied. This occurs when $E_{res} = E^{m}_{peak}$. This gives the condition [39,40,66]:

$$[\rho L]^{max}_{\mu e} \simeq \frac{(2p+1)\pi 5.18\times 10^3}{\tan 2\theta_{13}}\ \mathrm{Km\ gm/}cc. \quad (7)$$

Here, p takes integer values. This condition is independent of Δ_{31} but depends sensitively on θ_{13}. ρ in Eq. (7) is the average density of matter along the path of travel. For trajectories passing through Earth's core, ρ strongly depends on the path length. In Fig. 1, we plotted ρL vs L for path lengths varying between 700 to 12 740 Km based on PREM profile of Earth density distribution. *In this paper, the symbol ρ refers to the value of earth matter density obtained from Fig.* 1, *for any value of L.* We identify the particular values of ρL which satisfy Eq. (7) with p = 0 for three different values of $\sin^2 2\theta_{13}$. *These occur at* L $\simeq$ 10 200 Km, *7600 Km, and 11 200 Km for* $\sin^2 2\theta_{13} = 0.1$ 0.2, *and* 0.05 *respectively.* This identifies the baselines at which $P^{m}_{\mu e}$ is maximized. Additionally, the relatively wide spacing between them demonstrates the sensitivity to θ_{13}.

[4]Note that this condition is sensitive to the sign of Δ_{31}. $\Delta_{31} > 0$ gives rise to matter enhancement in case of neutrinos, while for antineutrinos (since $A \rightarrow -A$) one gets a suppression due to matter effects. The situation is reversed for $\Delta_{31} < 0$.

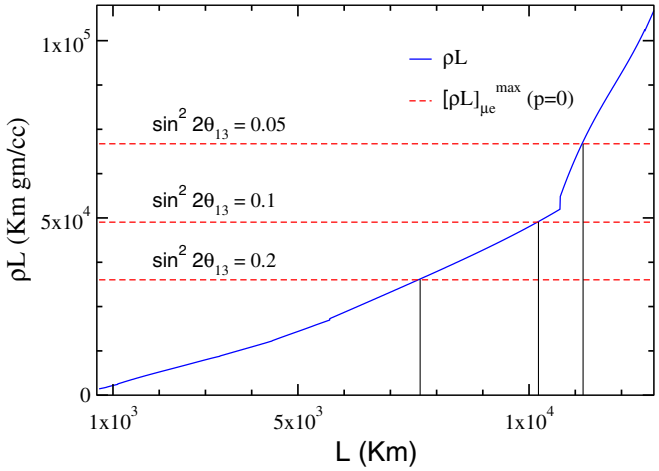

FIG. 1 (color online). ρL plotted vs L. Horizontal lines correspond to $[\rho L]^{max}_{\mu e}$ for different values of θ_{13} calculated using Eq. (7) for $p = 0$.

At and around the resonant energies and these baselines (depending on the value of θ_{13}) $P^{m}_{\mu e}$ significantly impacts not only $P_{\mu\mu}$, but also $P_{\mu\tau}$, as we discuss below. Note that for higher values of p, the baselines for maximum matter effect are greater than the Earth's diameter. Hence p = 0 is the only relevant value of p in this case.

B. Matter effects in $P_{\mu\tau}$

In vacuum we have

$$P^{v}_{\mu\tau} = \cos^4\theta_{13}\sin^2 2\theta_{23}\sin^2(1.27\Delta_{31}L/E),$$
$$= \cos^2\theta_{13}\sin^2 2\theta_{23}\sin^2(1.27\Delta_{31}L/E) - \cos^2\theta_{23}P^{v}_{\mu e}. \quad (8)$$

Including the matter effects changes this to

$$P^{m}_{\mu\tau} = \cos^2\theta^{m}_{13}\sin^2 2\theta_{23}\sin^2[1.27(\Delta_{31} + A + \Delta^{m}_{31})L/2E]$$
$$+ \sin^2\theta^{m}_{13}\sin^2 2\theta_{23}\sin^2[1.27(\Delta_{31} + A - \Delta^{m}_{31})L/2E]$$
$$- \cos^2\theta_{23}P^{m}_{\mu e}. \quad (9)$$

Compared to $P^{m}_{\mu e}$, these expressions have a more complex matter dependence. This occurs due to the more complicated change of ν_μ and ν_τ in the flavor content of the matter dependent mass eigenstates. Labeling the vacuum mass eigenstates as ν_1, ν_2, and ν_3, in the approximation where $\Delta_{21} = 0$, ν_1 can be chosen to be almost entirely ν_e and ν_2 to have *no* ν_e component. Inclusion of the matter term A leaves ν_2 untouched but gives a nonzero matter dependent mass to ν_1, thereby breaking the degeneracy of the two mass states. As the energy increases, the ν_e component of ν^{m}_1 decreases and the ν_μ, ν_τ components increase such that at resonance energy they are 50%. Similarly, increasing energy increases the ν_e component of ν^{m}_3 (and reduces the ν_μ, ν_τ components) so that at resonance it becomes 50%. Thus in the resonance region,

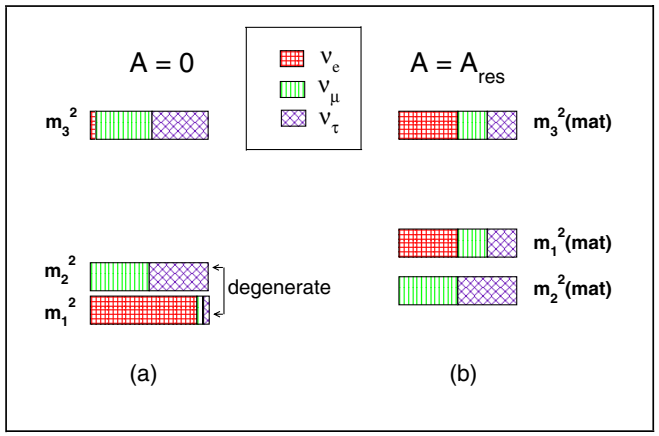

FIG. 2 (color online). The flavor composition of mass eigenstates in vacuum (A = 0) and in matter at resonance ($A = A_{res}$). The vacuum parameters used are $\sin^2 2\theta_{23} = 1.0$ and $\sin^2 2\theta_{13} = 0.1$.

all three matter dependent mass eigenstates ν_1^m, ν_2^m, and ν_3^m contain significant ν_μ and ν_τ components. Hence, the matter dependent $\nu_\mu \rightarrow \nu_\tau$ oscillation probability will depend on all three matter modified mass-squared differences. In Fig. 2 we show the flavor composition of the three mass states in vacuum and in matter at resonance.

We are interested in finding ranges of energy and path lengths for which there are large matter effects in $P_{\mu\tau}$, i.e., for which $\Delta P_{\mu\tau} = P^m_{\mu\tau} - P^v_{\mu\tau}$ is large. To this end, it is useful to examine the set of probability plots given in Fig. 3. The plots display the variation of $P^m_{\mu\tau}$ with neutrino energy E for baselines of 8000 Km, 9700 Km, and 10 500 Km, respectively, with each of the terms in Eq. (9) plotted separately. $P^m_{\mu\tau}(1)$, $P^m_{\mu\tau}(2)$, and $P^m_{\mu\tau}(3)$ in the figure refer to the first, second, and third term in Eq. (9), respectively, with the third term plotted incorporating its negative sign.

Additionally, the plots display the full vacuum probability, $P^v_{\mu\tau}$. The approximate average density at these baselines is $\rho \simeq 4.5$ gm/cc, hence one gets $E_{res} \simeq 5$ GeV from Eq. (6). The vacuum peaks, of course, shift with baseline and we see that a significantly broad peak gradually positions itself above the resonant energy at the baselines shown in the figure. We use this fact in Subsection II B 1 below.

We show that appreciable changes in $P^m_{\mu\tau}$ occur for two different sets of conditions, leading in one case to a sharp decrease from a vacuum maximum and in another to a smaller but extended increase over a broad range of energies. Both are discussed below in turn.

1. Large decrease in $P^m_{\mu\tau}$ in the resonance region

As is evident in Fig. 3, at energies appreciably below resonance, term 1 in Eq. (9) (i.e. the one with $\cos^2\theta^m_{13}$) is very nearly equal to $P^v_{\mu\tau}$. This is because $\theta^m_{13} = \theta_{13}$, $A \ll \Delta_{31}$, $\Delta^m_{31} \simeq \Delta_{31}$. Term 2, the $\sin^2\theta^m_{13}$ term, is nearly zero.

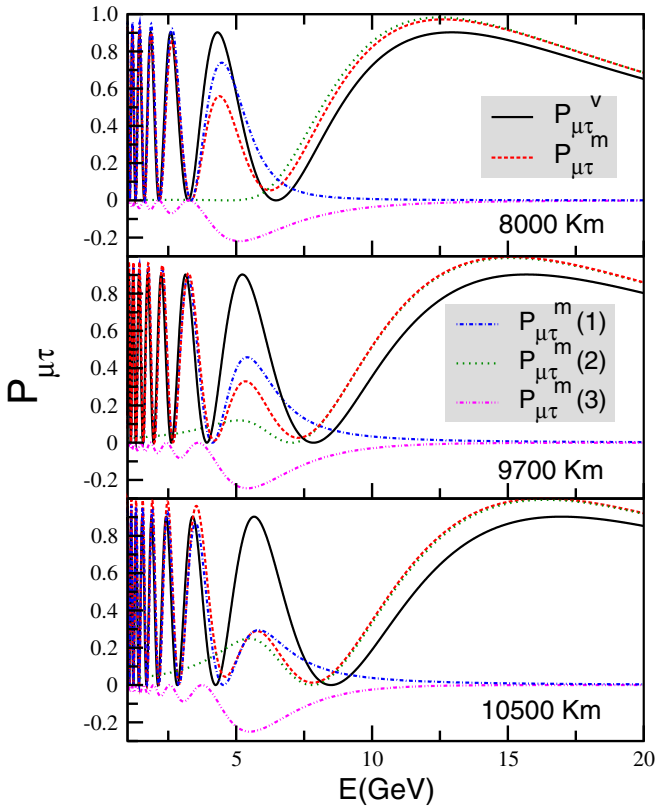

FIG. 3 (color online). The variation of $P_{\mu\tau}$ in matter ($P^m_{\mu\tau}$) and in vacuum ($P^v_{\mu\tau}$) with neutrino energy E for three different baselines of 8000 Km, 9700 Km, and 10 500 Km, respectively. Here we have used an approximate average density $\simeq 4.5$ gm/cc. Each of the terms in Eq. (9) also are shown in the three plots: $P^m_{\mu\tau}(1)$ is term 1, $P^m_{\mu\tau}(2)$ is term 2, and $P^m_{\mu\tau}(3)$ is term 3, respectively.

Similarly, term 3 is also very small. As we increase the energy and approach resonance, $\cos^2\theta^m_{13}$ begins to decrease sharply, deviating from its vacuum values, while $\sin^2\theta^m_{13}$ increases rapidly. However, *if resonance is in the vicinity of a vacuum peak*, which is the case at and around the baselines shown in Fig. 3, then the decrease in the $\cos^2\theta^m_{13}$ term has a much stronger impact on $P^m_{\mu\tau}$ than the increase in the $\sin^2\theta^m_{13}$ term, since the latter starts out at zero while the former is initially close to its peak value (~ 1). As a result, $P^m_{\mu\tau}$ falls sharply. This fall is enhanced by the third term in Eq. (9), which is essentially $0.5 \times P^m_{\mu e}$ (which is large due to resonance), leading to a large overall drop in $P^m_{\mu\tau}$ from its vacuum value. Note that the requirement that we be at a vacuum peak to begin with forces $\Delta P_{\mu\tau}$ to be large and negative, with the contributions from the first and the third term reinforcing each other.

The criterion for a maximal matter effect, $E_{res} \simeq E^v_{peak}$, leads to the following condition:

$$[\rho L]^{max}_{\mu\tau} \simeq (2p + 1)\pi 5.18 \times 10^3 (\cos 2\theta_{13}) \text{ Km gm}/cc. \quad (10)$$

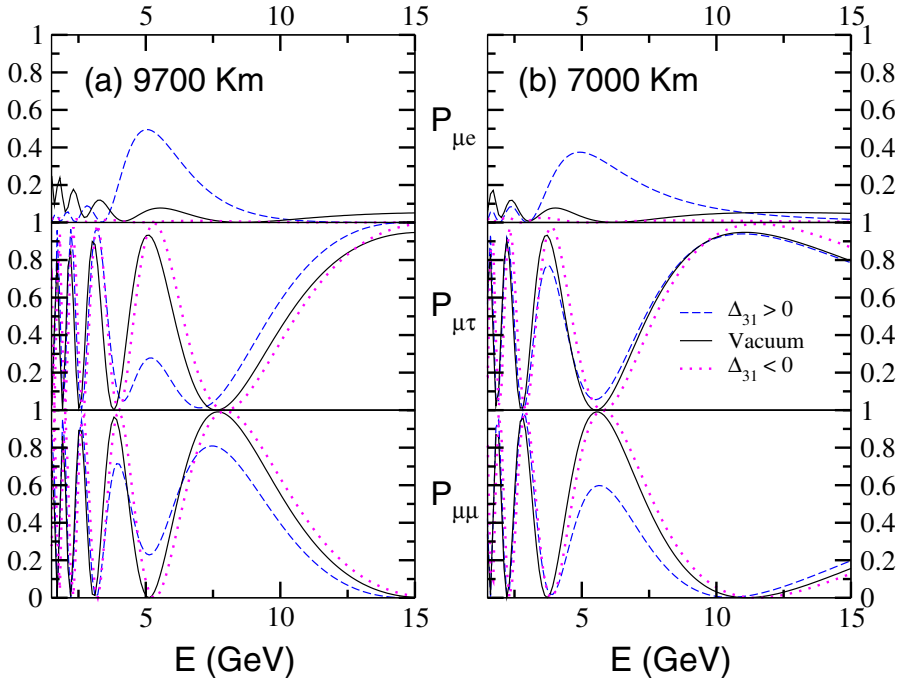

FIG. 4 (color online). $P_{\mu\tau}$ and $P_{\mu\mu}$ plotted as a function of neutrino energy, E (in GeV) in presence of matter and in vacuum for both signs of Δ_{31} for two different baseline lengths, (a) for L = 9700 Km and (b) for L = 7000 Km. These plots use $\Delta_{31} = 0.002$ eV^2 and $\sin^2 2\theta_{13} = 0.1$.

Unlike Eq. (7), which has a $\tan 2\theta_{13}$ in its denominator, Eq. (10) has a much weaker dependence on θ_{13}.

From Eq. (8) and Eq. (9), we write

$$\begin{aligned}\Delta P_{\mu\tau} &= P^{m}_{\mu\tau} - P^{v}_{\mu\tau} \\ &= \sin^2 2\theta_{23}[-\cos^4\theta_{13}\sin^2(1.27\Delta_{31}L/E) \\ &\quad + \cos^2\theta^{m}_{13}\sin^2[1.27(\Delta_{31} + A + \Delta^{m}_{31})L/2E] \\ &\quad + \sin^2\theta^{m}_{13}\sin^2[1.27(\Delta_{31} + A - \Delta^{m}_{31})L/2E] \\ &\quad - \sin^2\theta^{m}_{13}\cos^2\theta^{m}_{13}\sin^2(1.27\Delta^{m}_{31}L/E)]. \end{aligned} \tag{11}$$

Incorporating the $E_{res} \simeq E^{v}_{peak}$ condition [Eq. (10)] leads to

$$\Delta P_{\mu\tau} \simeq \cos^4\left[\sin 2\theta_{13}(2p+1)\frac{\pi}{4}\right] - 1. \tag{12}$$

We note that, in general, $\Delta P_{\mu\tau}$ (at $E_{res} \simeq E^{v}_{peak}$) will be larger for higher values of both p and θ_{13}. For p = 1 and $\sin^2 2\theta_{13} = 0.1$, $E_{res} \simeq E^{v}_{peak}$ occurs at ~9700 Km [from Eq. (10)] and $\Delta P_{\mu\tau} \sim -0.7$ [from Eq. (12)]. For p = 0, Eq. (10) gives $L^{max}_{\mu\tau} \sim 4400$ Km for $\sin^2 2\theta_{13} = 0.1$. However, $\Delta P_{\mu\tau}$ is roughly one-tenth of the p = 1 case. In general, for a given baseline, the choice of an optimal p is also dictated by the constraint that the vacuum peak near resonance have a breadth which makes the effect observationally viable. Note that for $\sin^2 2\theta_{13} = 0.05$ and 0.2, Eq. (10) gives the distances of maximum matter effect as ~9900 and 9300 Km for p = 1. Because of the weaker dependence on θ_{13} here compared to $P^{m}_{\mu e}$ [Eq. (7)], the distances for various values of θ_{13} are bunched together in the vicinity of 9500 Km.

In Fig. 4(a), we show all three matter and vacuum probabilities for 9700 Km. In these plots Δ_{31} is taken as 0.002 eV^2 which gives $E_{res} \simeq E^{v}_{peak}$ at 5 GeV. The middle panel of Fig. 4(a) shows that near this energy $P^{m}_{\mu\tau}$ (~ 0.33) is appreciably lower compared to $P^{v}_{\mu\tau}$ (~ 1). Thus the drop due to matter effect is 0.67, which agrees well with that obtained in the paragraph above using the approximate expression Eq. (12).

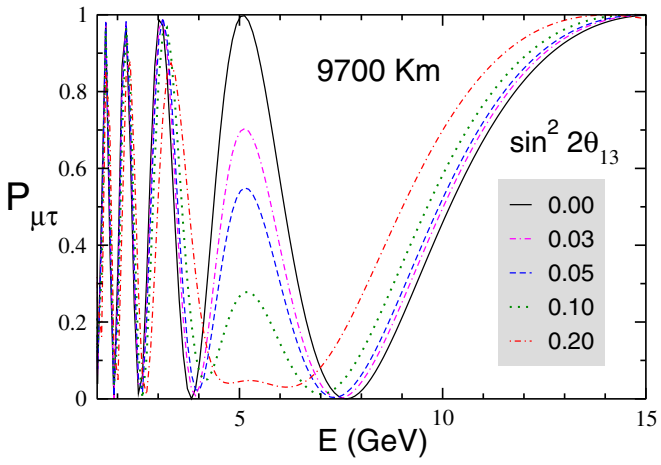

FIG. 5 (color online). The plot shows sensitivity to θ_{13} in case of $P_{\mu\tau}$ for a baseline length of 9700 Km. The value of Δ_{31} is taken to be 0.002 eV^2.

In Fig. 5 we show the θ_{13} sensitivity of $P^m_{\mu\tau}$ at 9700 Km.[5] In particular, at $E_{res} \simeq E^v_{peak}$ the strong dependence on θ_{13} is also governed by Eq. (12) above. Thus we have significant change in $P^m_{\mu\tau}$ due to matter effects, even for small values of θ_{13}. This is illustrated in Fig. 5, where we see that, even for as small a value of $\sin^2 2\theta_{13} = 0.03$, matter effects at maximal resonance cause a change in $P^m_{\mu\tau}$ of about 30%. This amplification of matter effects at resonance occurs for similar path lengths for all allowed values of θ_{13}, as given in [Eq. (10)]. This is to be contrasted with the case of $\nu_\mu \rightarrow \nu_e$ oscillations, where the observation of resonance amplification is possible only for θ_{13} close to the present upper bound. Actual observation of these maximal resonance matter effects in the $\nu_\mu \rightarrow \nu_\tau$ oscillations will be very difficult, because of the smallness of cross sections and the difficulty in reconstructing the τ. With a very high intensity source, such as a neutrino factory and a specialized τ detector, it may be possible. A study of this will be reported elsewhere [67].

2. Increase in $P^m_{\mu\tau}$ away from resonance

We now discuss the second scenario for which $P^m_{\mu\tau}$ can differ appreciably from $P^v_{\mu\tau}$. This happens away from resonance, and is evident in Fig. 4(a) (central panel) in the energy range 7.5–15 GeV. This effect is an enhancement rather than a drop, i.e., $\Delta P_{\mu\tau}$ is now positive, unlike the previous case.

$\Delta P_{\mu e}$ is small in most of the latter part of the energy region under consideration and does not contribute in an important way overall [Fig. 4(a) (top panel)]. The dominant contribution to this enhancement arises from the $\sin^2\theta^m_{13}$ term in $P^m_{\mu\tau}$ [(Eq. (9)] which is large for $E \gg E_{res}$. Since $(\Delta_{31} + A - \Delta^m_{31}) \simeq 2\Delta_{31}$ for these energies, we obtain an enhancement ($\sim 15\%$) which follows the vacuum curve. The difference between the two curves, vacuum and matter, largely reflects the difference between the $\cos^4\theta_{13}$ multiplicative term in the vacuum expression Eq. (8) and the $\sin^2\theta^m_{13}$ multiplicative term in Eq. (9). While this effect is smaller compared to the effect discussed in Subsection II B 1 above, it occurs over a broad energy band and can manifest itself in energy integrated event rates.

C. Matter effects in $P_{\mu\mu}$

In vacuum $P_{\mu\mu}$ is given by

$$\begin{aligned} P^v_{\mu\mu} &= 1 - P^v_{\mu\tau} - P^v_{\mu e} \\ &= 1 - \cos^4\theta_{13}\sin^2 2\theta_{23}\sin^2(1.27\Delta_{31}L/E) \\ &\quad - \sin^2\theta_{23}\sin^2 2\theta_{13}\sin^2(1.27\Delta_{31}L/E). \end{aligned} \tag{13}$$

Including the matter effects changes this to

$$\begin{aligned} P^m_{\mu\mu} &= 1 - P^m_{\mu\tau} - P^m_{\mu e} \\ &= 1 - \cos^2\theta^m_{13}\sin^2 2\theta_{23}\sin^2[1.27(\Delta_{31} + A + \Delta^m_{31})L/2E] \\ &\quad - \sin^2\theta^m_{13}\sin^2 2\theta_{23}\sin^2[1.27(\Delta_{31} + A - \Delta^m_{31})L/2E] \\ &\quad - \sin^4\theta_{23}\sin^2 2\theta^m_{13}\sin^2(1.27\Delta^m_{31}L/E). \end{aligned} \tag{14}$$

The deviation of $P^m_{\mu\mu}$ from $P^v_{\mu\mu}$ clearly results from the combined effects in $P^m_{\mu\tau}$ and $P^m_{\mu e}$. In order to quantify the extent of deviation, we define,

$$\Delta P_{\mu\mu} = -\Delta P_{\mu\tau} - \Delta P_{\mu e}. \tag{15}$$

Below we illustrate the various conditions which can give rise to a significant change in $P_{\mu\mu}$ due to matter effects arising in both $P_{\mu\tau}$ and $P_{\mu e}$:

(a) *Large, negative* $\Delta P_{\mu\tau}$ *and positive* $\Delta P_{\mu e}$.—Large and negative $\Delta P_{\mu\tau}$ corresponds to the case discussed in Subsection II B 1. In this case, $\Delta P_{\mu e}$ is positive, so the signs of the two changes are opposite and hence the two terms [Eq. (15)] do not contribute in consonance. However, the resulting *increase* in $P_{\mu\mu}$ is still significant ($\sim 20\%$), given the magnitude of the change ($\sim 70\%$) in $P_{\mu\tau}$. This is visible in the bottom panel of Fig. 4(a), in the energy range 4–6 GeV.

(b) *Positive* $\Delta P_{\mu\tau}$ *and small* $\Delta P_{\mu e}$.—This case corresponds to a significant *drop* in $P^m_{\mu\mu}$, which is seen in Fig. 4(a) (bottom panel) in the energy range $\sim$7–15 GeV. The enhancement in $P^m_{\mu\tau}$ (corresponding to the case discussed in Subsection II B 2) is reflected in the decrease in $P^m_{\mu\mu}$ compared to its vacuum value.

(c) *Small* $\Delta P_{\mu\tau}$ *and large, positive* $\Delta P_{\mu e}$.—This situation occurs when a minimum in the vacuum value of $P_{\mu\tau}$ resides in the proximity of a resonance. The condition for a minimum in $P_{\mu\tau}$ is $1.27\Delta_{31}L/E = p\pi$. In this region, the rapidly changing $\sin^2\theta^m_{13}$ and $\cos^2\theta^m_{13}$ increase $P_{\mu\tau}$ from its vacuum value of 0 to about 0.1. At the same time, $P_{\mu e}$ undergoes an increase of 0.3, thus leading to a net change of $P_{\mu\mu} = 0.4$ [the three panels of Fig. 4(b)]. Note that the above condition corresponds to a vacuum peak of $P_{\mu\mu}$ and the 40% drop of its value makes this energy range (4–10 GeV) suitable for searching for matter effects. Substituting E as E_{res} gives the distance for maximum matter effect in $P_{\mu\mu}$ as

$$[\rho L]^{max}_{\mu\mu} \simeq p\pi \times 10^4(\cos 2\theta_{13}) \text{ Km gm}/cc. \tag{16}$$

For $p = 1$, this turns out to be $\sim$7000 Km.[6] This effect [59] is shown in the bottom panel of Fig. 4(b). The large (40% at its peak) drop in $P^m_{\mu\mu}$ seen in this figure derives its strength mainly from the resonant

[5] $P^m_{\mu\tau}$ develops good sensitivity to θ_{13} only at around L = 9700 Km. As shown in the middle panel of 4(b), even at L = 7000 Km, its sensitivity to matter effects is relatively poor [59].

[6] Note that this length is close to the "magic baseline" [68,69].

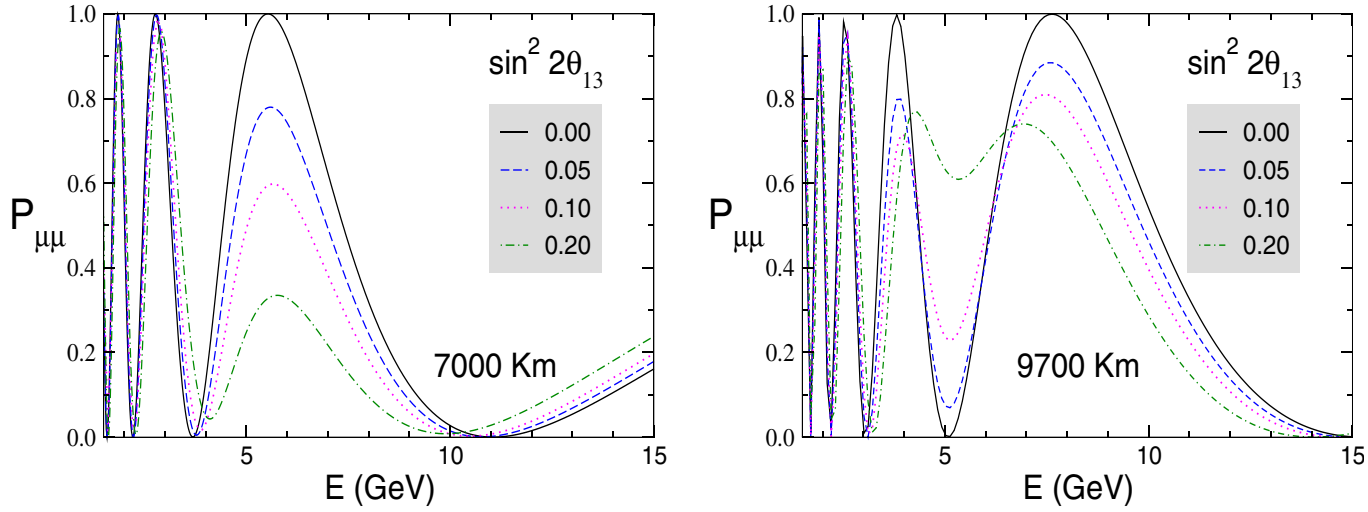

FIG. 6 (color online). Figure (a) and (b) depict $P_{\mu\mu}$ in matter plotted against the neutrino energy E (in GeV) for different values of θ_{13} and two baseline lengths, viz., 7000 Km and 9700 Km, respectively.

enhancement in $P^{m}_{\mu e}$.

Defining $\Delta P_{\mu\mu} = P^{m}_{\mu\mu} - P^{v}_{\mu\mu}$ and incorporating the condition that $E_{res} \simeq E^{v}_{peak}$ of $P_{\mu\mu}$ [Eq. (16)] leads to

$$\Delta P_{\mu\mu} \simeq -\sin^2\left[\sin 2\theta_{13} p \frac{\pi}{2}\right] - 0.25\sin^2[\sin 2\theta_{13} p \pi]. \quad (17)$$

The θ_{13} sensitivity of $P^{m}_{\mu\mu}$ for L = 7000 Km and for L = 9700 Km is shown in Fig. 6. In Fig. 6(a), we see that for L = 7000 Km, the maximum θ_{13} sensitivity is in the energy range 4–10 GeV. Our ability to observe this drop in $P^{m}_{\mu\mu}$ depends on the statistics. The condition for 3σ observability may be stated as

$$N_{\mu}(\theta_{13} = 0) - N_{\mu}(\theta_{13}) \geq 3\sqrt{N_{\mu}(\theta_{13})}. \quad (18)$$

Figure 7 depicts the sensitivity of $P^{m}_{\mu\mu}$ to θ_{23} for the same distances, showing a similar inverse relation between the survival probability and the value of θ_{23}. Note that, for these baselines, $P_{\mu\mu}$ changes by as much as 20%, for the

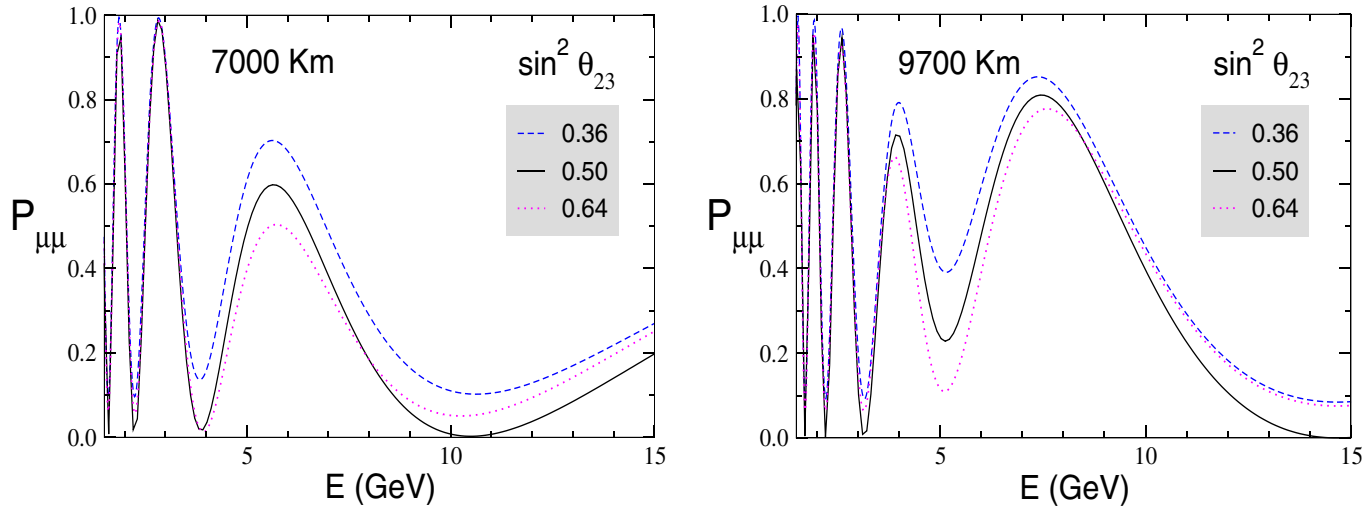

FIG. 7 (color online). Figure (a) and (b) depict $P_{\mu\mu}$ in matter plotted vs E (in GeV) for different values of θ_{23} and two baseline lengths, viz., 7000 Km and 9700 Km, respectively, for $\sin^2 2\theta_{13} = 0.1$. The value of Δ_{31} is taken to be 0.002 eV^2.

currently allowed range of θ_{23}. A criterion similar to Eq. (18) can be applied to these sensitivities in situations where their observability is feasible. This is likely to happen in long baseline experiments with high luminosity sources.

The width of the effects discussed above for $P_{\mu\mu}$ is significant, ranging from 4–6 GeV in case (a), 7–15 GeV in case (b) [Fig. 4(a)] and 4–10 GeV in case (c) [Fig. 4(b)]. We have checked that they persist over a range of baselines (6000–10 500 Km), making them observationally feasible, as is demonstrated later.

In general the resonance has a width, and this fact affects observability. Below we give an expression for $\Delta P_{\mu\mu}$ which incorporates the resonance width and thus quantifies the deviation between E_{res} and E^{ν}_{peak} which can exist while still keeping the effect observable. To include the width of the resonance, we write $A = \Delta_{31}(\cos 2\theta_{13} + q\sin 2\theta_{13})$, where q varies from -1 to 1. With this parametrization,

$$\begin{aligned}\Delta P_{\mu\mu} = &-Q_{+}\sin^2\left[1.27\frac{\Delta_{31}L}{E}\left(1-\sin 2\theta_{13}\frac{\sqrt{q^2+1}-q}{2}\right)\right]\\ &-Q_{-}\sin^2\left[1.27\frac{\Delta_{31}L}{E}\left(1+\sin 2\theta_{13}\frac{\sqrt{q^2+1}+q}{2}\right)\right]\\ &-1/[4(q^2+1)]\sin^2\left[1.27\frac{\Delta_{31}L}{E}\left(\sin 2\theta_{13}\sqrt{q^2+1}\right)\right]\\ &+\sin^2(1.27\Delta_{31}L/E). \qquad (19)\end{aligned}$$

Here, $Q_{\pm} = (\sqrt{q^2+1} \pm q)/(2\sqrt{q^2+1})$. In obtaining Eq. (19) we have approximated $\cos 2\theta_{13}, \cos^2\theta_{13} \simeq 1$.

D. Degeneracies in the determination of oscillation parameters at very long baselines

In our analytic discussion of matter effects on oscillation probabilities, we have used approximate expressions with the solar mass-squared difference Δ_{21} set to zero. While this is adequate for a broad understanding of matter effects, it is interesting to look at a more accurate picture with $\Delta_{21} \neq 0$ and analyze the issue of parameter degeneracies associated with the inclusion of subleading effects. In this situation, the determination of neutrino mass and mixing parameters is complicated by the presence of degeneracies in the oscillation probabilities, which are inherent in a three generation analysis due to the presence of the nonzero *CP* phase δ_{CP}. The degeneracies, extensively studied in the literature for baselines less than 3000 Km, are *the* $(\delta_{CP}, \theta_{13})$ *ambiguity, the sign* (Δ_{31}) *or mass hierarchy degeneracy and the* $(\theta_{23}, \pi/2 - \theta_{23})$ *or atmospheric angle degeneracy, combining to give an overall eight-fold degeneracy* [68,70–72]. It is relevant to discuss briefly the effect of parameter degeneracies in the context of very long baselines, as are considered in this paper.

The analytic treatment of degeneracies is based on approximate expressions for the oscillation probabilities in matter of constant density. These are computed by series expansions in the small parameters—the solar mass-squared difference Δ_{21} and the mixing angle θ_{13}. *CP* trajectory orbits in biprobability space are widely used for depicting degeneracies, and are conventionally plotted using the analytic expressions. For the purpose of the biprobability calculations here, analytic expressions become progressively inadequate beyond 4000 Km, or more precisely, for values of L and E such that $L/E \geq 10^4$ Km/GeV. Additionally, the small θ_{13} expansion also fails for relatively large values of θ_{13} (close to the present CHOOZ bound). In view of this, we have plotted the *CP* trajectories for a sample long baseline using the full numerical solution of the evolution equation with earth matter effects. However, the analytic expressions remain useful for a qualitative understanding of the features and interdependence of parameter degeneracies, and we use them for this purpose whenever necessary.

The approximate analytic expressions for oscillation probability between two flavors α, β are of the form [61,71]

$$P_{\alpha\beta} = X_{\alpha\beta}\cos\delta_{CP} + Y_{\alpha\beta}\sin\delta_{CP} + Z_{\alpha\beta}, \qquad (20)$$

where $X_{\alpha\beta}$, $Y_{\alpha\beta}$, and $Z_{\alpha\beta}$ are functions of the neutrino mass-squared differences and mixing parameters but independent of the *CP* phase δ_{CP}. Note that $Z_{\alpha\beta}$ contains the dominant contribution to the probabilities given earlier [Eqs. (3), (4), (8), (9), (13), and (14)]. It can be shown that the generic form of a *CP* trajectory in biprobability space [the orbit traced in $(P_{\alpha\beta}, \bar{P}_{\alpha\beta})$ space as δ_{CP} varies from 0 to 2π] is an ellipse [71], which collapses to a line under certain conditions.

Here $\bar{P}_{\alpha\beta}$ is the *CP* conjugated (antineutrino) probability. Specific expressions for $P^{m}_{\mu e}$, $P^{m}_{\mu\tau}$, and $P^{m}_{\mu\mu}$ may be found in [64]. The small Δ_{21}, small θ_{13} series expansions (to second order in these parameters) are compact and hence easier to analyze for degeneracies. Below we list the expressions for the coefficients $X_{\alpha\beta}$ and $Y_{\alpha\beta}$ in this approximation for $P^{m}_{\mu e}$ and $P^{m}_{\mu\tau}$:

$$\begin{aligned}X_{\mu e} &= 2\alpha\sin\theta_{13}\sin 2\theta_{12}\sin 2\theta_{23}\cos\Delta\frac{\sin\hat{A}\Delta}{\hat{A}}\frac{\sin(\hat{A}-1)\Delta}{(\hat{A}-1)},\\ Y_{\mu e} &= -2\alpha\sin\theta_{13}\sin 2\theta_{12}\sin 2\theta_{23}\sin\Delta\frac{\sin\hat{A}\Delta}{\hat{A}}\frac{\sin(\hat{A}-1)\Delta}{(\hat{A}-1)},\\ X_{\mu\tau} &= -\frac{2}{\hat{A}-1}2\alpha\sin\theta_{13}\sin 2\theta_{12}\sin 2\theta_{23}\cos 2\theta_{23}\\ &\quad\times\sin\Delta\left[\hat{A}\sin\Delta - \frac{\sin\hat{A}\Delta}{\hat{A}}\cos(\hat{A}-1)\Delta\right],\\ Y_{\mu\tau} &= 2\alpha\sin\theta_{13}\sin 2\theta_{12}\sin 2\theta_{23}\sin\Delta\frac{\sin\hat{A}\Delta}{\hat{A}}\frac{\sin(\hat{A}-1)\Delta}{(\hat{A}-1)},\end{aligned} \qquad (21)$$

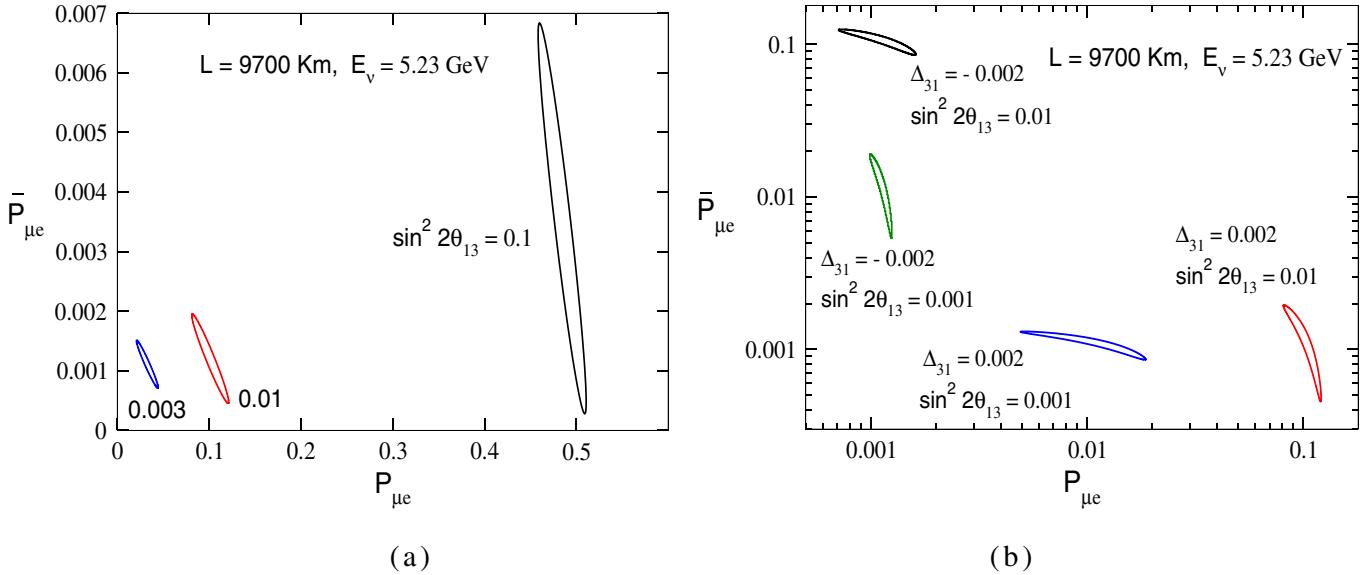

FIG. 8 (color online). (a) *CP* trajectory orbits in ($P_{\mu e}$, $\bar{P}_{\mu e}$) biprobability space with E = 5.23 GeV, L = 9700 Km ($1.27\Delta_{31}L/E = 3\pi/2$). Orbits with different values of θ_{13} do not overlap, showing that the (δ_{CP}, θ_{13}) degeneracy is resolved for these values of L and E. (b) *CP* trajectory plots in ($P_{\mu e}$, $\bar{P}_{\mu e}$) biprobability space for two different values of θ_{13} and both signs of Δ_{31}. Orbits with positive and negative Δ_{31} do not coincide, showing that the sign(Δ_{31}) degeneracy is resolved for this L and E till θ_{13} as low as $\sin^2 2\theta_{13} = 0.001$.

where $\Delta = 1.27\Delta_{31}L/E$, $\hat{A} = A/|\Delta_{31}|$, $\alpha = |\Delta_{21}|/|\Delta_{31}|$. The above expressions are for the normal mass hierarchy. For the inverted hierarchy, the transformations $\hat{A} \to -\hat{A}$, $\alpha \to -\alpha$, and $\Delta \to -\Delta$ are required. The coefficients for $P^m_{\mu\mu}$ are given by $X_{\mu\mu} = -X_{\mu e} - X_{\mu\tau}$, and similarly for $Y_{\mu\mu}$. Note that $Y_{\mu\mu} = 0$ and hence the survival probability is independent of the *CP*-odd term. Next we discuss in turn each of the possible degeneracies.

(i) The (δ_{CP}, θ_{13}) *degeneracy* arises when different pairs of values of the parameters δ_{CP} and θ_{13} give the same neutrino and antineutrino oscillation probabilities, assuming other parameters to be known and fixed. This may be expressed as

$$\begin{aligned} P_{\alpha\beta}(\delta_{CP}, \theta_{13}) &= P_{\alpha\beta}(\delta'_{CP}, \theta'_{13}), \\ \bar{P}_{\alpha\beta}(\delta_{CP}, \theta_{13}) &= \bar{P}_{\alpha\beta}(\delta'_{CP}, \theta'_{13}). \end{aligned} \tag{22}$$

This ambiguity manifests itself in the intersection of *CP* orbits with different values of θ_{13}. The intersection points indicate the different values of δ_{CP} and θ_{13} for which the above Eq. (22) are satisfied. For values of L and E such that $\Delta = n\pi/2$, Eq. (21) predict that either $\sin\delta_{CP}$ or $\cos\delta_{CP}$ drops out of the expression for $P^m_{\mu e}$, reducing the *CP* trajectory to a straight line. Further, it can be shown that the (δ_{CP}, θ_{13}) ambiguity reduces in this case to a simple (δ_{CP}, $\pi - \delta_{CP}$) or (δ_{CP}, $2\pi - \delta_{CP}$) ambiguity which does not mix different values of θ_{13} [68]. This fact holds true at long baselines also, as is depicted in Fig. 8(a) for L = 9700 Km, E = 5.23 GeV (giving $\Delta = 3\pi/2$). Here the *CP* orbits appear as widely separated narrow ellipses, showing that the (δ_{CP}, θ_{13}) ambiguity is effectively resolved.[7] *CP* orbit diagrams for $P^m_{\mu\mu}$ and $P^m_{\mu\tau}$ are given in Figs. 9(a) and 10(a), illustrating a similar lifting of the degeneracy involving θ_{13} in both cases. The approximate expressions [Eq. (21)] show that the muon neutrino survival probability is a function only of the *CP*-even term $\cos\delta_{CP}$, while $P^m_{\mu\tau}$ only depends on $\sin\delta_{CP}$ when θ_{23} is maximal, so their *CP* orbits resemble straight lines instead of ellipses.

(ii) The *mass hierarchy degeneracy* occurs due to identical solutions for P and $\bar{P}$ for different pairs of δ_{CP} and θ_{13} with opposite signs of Δ_{31} (again fixing other parameters):

$$\begin{aligned} P_{\alpha\beta}(\Delta_{31} > 0, \delta_{CP}, \theta_{13}) &= P_{\alpha\beta}(\Delta_{31} < 0, \delta'_{CP}, \theta'_{13}), \\ \bar{P}_{\alpha\beta}(\Delta_{31} > 0, \delta_{CP}, \theta_{13}) &= \bar{P}_{\alpha\beta}(\Delta_{31} < 0, \delta'_{CP}, \theta'_{13}). \end{aligned} \tag{23}$$

Note that a combined effect of the (δ_{CP}, θ_{13}) ambiguity and the sign (Δ_{31}) degeneracy gives rise to a four-fold degeneracy. From the expression for $P^m_{\mu e}$, it has been determined [68] that the condition for

[7]Here we have given a theoretical discussion of degeneracies in probabilities and therefore not taken into account possible error bars in the experimental results for event rates, which, if large enough, may cause points on different θ_{13} orbits to overlap.

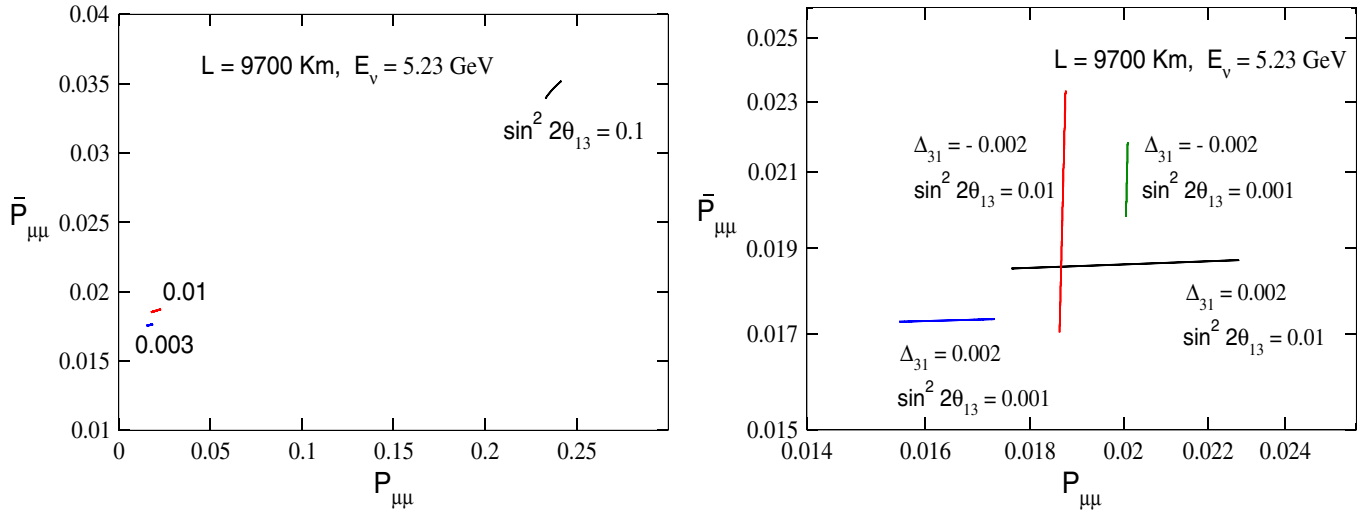

FIG. 9 (color online). Same as Fig. 8(a) and 8(b) but in ($P_{\mu\mu}$, $\bar{P}_{\mu\mu}$) biprobability space. In (b) the sign(Δ_{31}) degeneracy is present for $\sin^2 2\theta_{13} = 0.01$.

this ambiguity to be resolved is

$$\sin 2\theta_{13} > \frac{2\alpha \tan\theta_{23} \sin 2\theta_{12} \sin\hat{A}\Delta}{\hat{A}\left[\frac{\sin(1-\hat{A})\Delta}{1-\hat{A}} - \frac{\sin(1+\hat{A})\Delta}{1+\hat{A}}\right]}. \qquad (24)$$

This places constraints on θ_{13} as well as the baseline, which must be large enough for the denominator to be large (thus weakening the constraint on θ_{13}). Figure 8(b) gives the orbit diagram for the energy and baseline earlier discussed. It is seen that the orbit ellipses for positive and negative Δ_{31} are well separated for $\sin^2 2\theta_{13} = 0.001$. Thus the degeneracy is lifted even for very small values of θ_{13}. From Fig. 10(b), it is clear that $P^m_{\mu\tau}$ is also free from this ambiguity for large baselines. However, $P^m_{\mu\mu}$ shows a mass hierarchy degeneracy for $\sin^2 2\theta_{13} = 0.01$, as seen in Fig. 9(b).

(iii) Currently θ_{23} is determined from $P^v_{\mu\mu}$ in atmospheric (SK) and accelerator (K2K) experiments. Since this is a function of $\sin^2 2\theta_{23}$, these measurements cannot differentiate θ_{23} from $\pi/2 - \theta_{23}$. If the probability is a function of $\sin^2\theta_{23}$ or $\cos^2\theta_{23}$ (e.g. the leading contributions in $P_{\mu e}$ and $P_{e\tau}$, re-

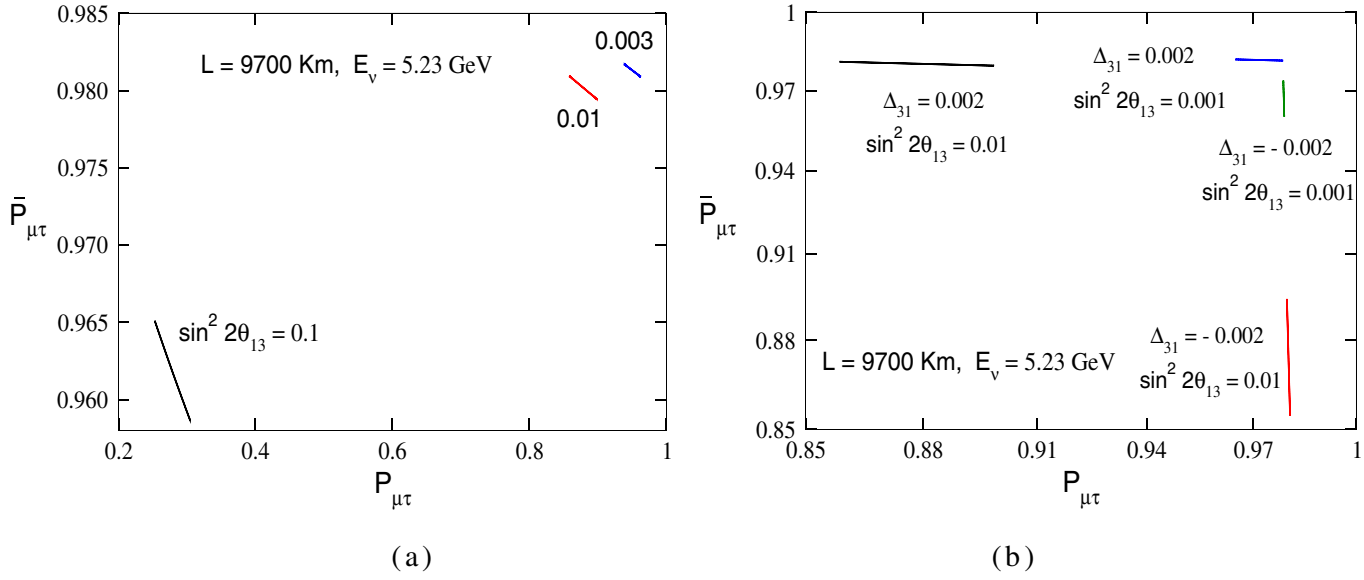

FIG. 10 (color online). Same as Fig. 8(a) and 8(b) but in ($P_{\mu\tau}$, $\bar{P}_{\mu\tau}$) biprobability space.

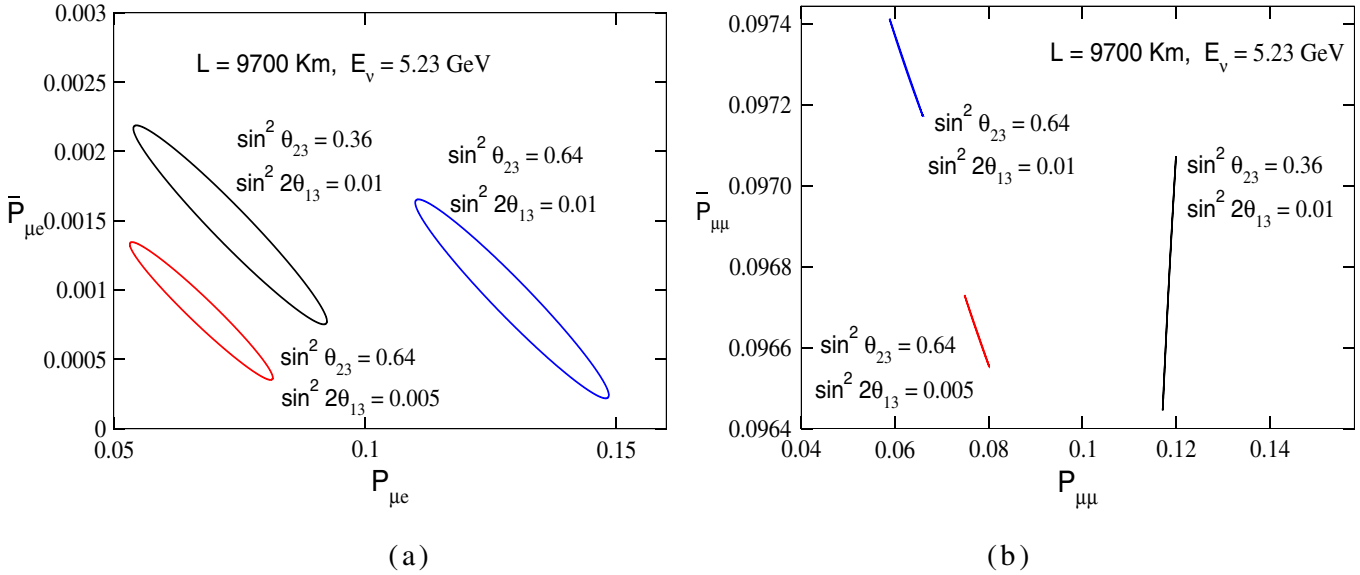

FIG. 11 (color online). (a) *CP* trajectory plots in $(P_{\mu e}, \bar{P}_{\mu e})$ biprobability space for different values of θ_{13} and complementary values of θ_{23}. (b) Same as Fig. 11(a) but in $(P_{\mu\mu}, \bar{P}_{\mu\mu})$ biprobability space.

spectively), then for a fixed value of θ_{13}, $P_{\alpha\beta}(\theta_{23}, \theta_{13}) \neq P_{\alpha\beta}(\pi/2 - \theta_{23}, \theta_{13})$. However, different values of θ_{13} and the *CP* phase δ_{CP} can make them equal[8], leading to an ambiguity in the determination of the latter two parameters known as the $(\theta_{23}, \pi/2 - \theta_{23})$ *degeneracy*:

$$P_{\alpha\beta}(\theta_{23}, \delta_{CP}\theta_{13}) = P_{\alpha\beta}(\pi/2 - \theta_{23}, \delta'_{CP}\theta'_{13}),$$
$$\bar{P}_{\alpha\beta}(\theta_{23}, \delta_{CP}\theta_{13}) = \bar{P}_{\alpha\beta}(\pi/2 - \theta_{23}, \delta'_{CP}\theta'_{13}). \quad (25)$$

The presence of this ambiguity along with the two previously discussed degeneracies will give rise to an eight-fold degeneracy [68] in such probabilities. However, if a probability is a function of $\sin^2 2\theta_{23}$ (e.g. $P_{\mu\tau}$), then for a fixed θ_{13}, $P_{\alpha\beta}(\theta_{23}, \theta_{13}) = P_{\alpha\beta}(\pi/2 - \theta_{23}, \theta_{13})$ to start with. Therefore, different values of θ_{13} and δ_{CP} give rise to different values of the probability, and the $(\theta_{23}, \pi/2 - \theta_{23})$ degeneracy will not lead to any further ambiguity in the determination of θ_{13}. So the total degeneracy in this case is four-fold.[9].

The *CP* trajectories for $P^m_{\mu e}$, $P^m_{\mu\mu}$, and $P^m_{\mu\tau}$ with complementary values of θ_{23} and our sample L and E are given in Figs. 11(a), 11(b), and 12. From Figs. 11(a) and 11(b), we see that the different θ_{23} orbits do not intersect, i.e. this degeneracy is resolved in $P^m_{\mu e}$ and $P^m_{\mu\mu}$ for a long baseline like the one discussed, even though in principle it could exist for these probabilities as they are functions of $\sin^2\theta_{23}$. However, in the case of $P^m_{\mu\tau}$, as discussed above, this degeneracy is absent since its approximate matter expression contains only $\sin^2 2\theta_{23}$ in its dominant terms. This feature is evident in Fig. 12. We see that all points on the orbits with complementary θ_{23} and equal θ_{13} coincide, so no two independent values of δ_{CP} can exist which give the same probability.

(iv) It also can be observed from the analytic expressions for $X_{\alpha\beta}$ and $Y_{\alpha\beta}$ [Eq. (21)] that the magic baseline scenario [68,69] discussed for $P^m_{\mu e}$ is equally valid for $P^m_{\mu\mu}$ and $P^m_{\mu\tau}$ when $\theta_{23} = \pi/4$. This method of degeneracy resolution requires the

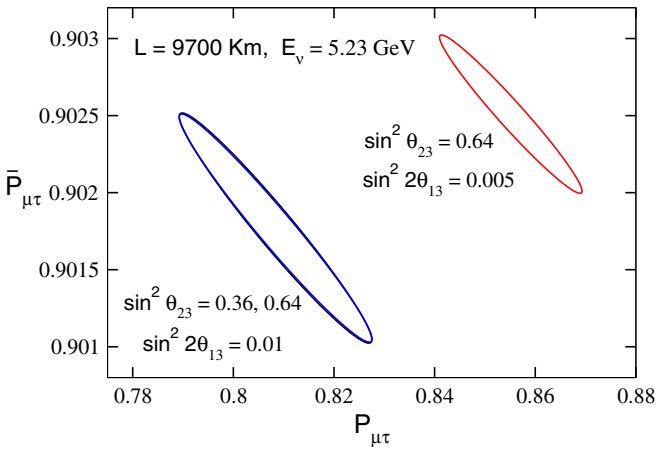

FIG. 12 (color online). Same as Fig. 9(a) but in $(P_{\mu\tau}, \bar{P}_{\mu\tau})$ biprobability space.

[8]This degeneracy may be present even if $\delta_{CP} = 0$.

[9]Note that probabilities that are functions of $\sin^2 2\theta_{23}$, though only four-fold degenerate with respect to θ_{13} and δ_{CP}, cannot ascertain whether $\theta_{23} < \pi/4$ or $\theta_{23} > \pi/4$. This information can be obtained from a comparison of probabilities which are functions of $\sin^2\theta_{23}$ and $\cos^2\theta_{23}$ (for e.g., the golden and silver channels discussed in [73,74]).

baseline to satisfy $\hat{A}\Delta = n\pi$, in which case all coefficients of δ_{CP} vanish. The energy and parameter-independent condition on L becomes $\rho L = 32\,532$ Km gm/cc. From the ρL vs L curve (Fig. 1), it is seen that this corresponds to L $\simeq$ 7600 Km. An identical analysis applies to $P^m_{\mu\mu}$ and $P^m_{\mu\tau}$ with maximal θ_{23}, with only a small correction if θ_{23} is nonmaximal.

In conclusion, we find that a study of probabilities at a baseline and energy like the one discussed demonstrates, in general, a breaking of most of the parameter degeneracies which can confuse the determination of θ_{13} from oscillation measurements. For $P_{\mu e}$, this is true for all three classes of degeneracies mentioned above. In the case of the muon survival probability, Fig. 9(b) shows that sign(Δ_{31}) may still be undetermined for specific values of θ_{13} and the CP phase δ_{CP}, for which the same value of ($P_{\mu\mu}$, $\bar{P}_{\mu\mu}$) are obtained with opposite signs of Δ_{31}. For example, for $\sin^2 2\theta_{13} = 0.01$, we have checked that $\delta_{CP} = 0.305\pi$ and $\delta_{CP} = 0.337\pi$ give the same point in ($P_{\mu\mu}$, $\bar{P}_{\mu\mu}$) space for positive and negative Δ_{31}, respectively, for L = 9700 Km and E = 5.23 GeV. In $P_{\mu\tau}$, all degeneracies involving a measurement of θ_{13} and δ_{CP} are lifted for the energy and baseline discussed. Also, we note that the maximum total degeneracy of $P_{\mu\tau}$ is four fold even in principle, since its analytic expression in matter (to second order in the expansion parameters) is a function of $\sin 2\theta_{23}$.

III. DETERMINING THE MASS HIERARCHY VIA ATMOSPHERIC ν_μ IN A CHARGE DISCRIMINATING DETECTOR

In the discussion in Secs. II A, II B, and II C, we have shown that large matter effects in neutrino oscillations are not necessarily confined to $\nu_\mu \to \nu_e$ or $\nu_e \to \nu_\tau$ conversions but can be searched for in $\nu_\mu \to \nu_\tau$ oscillation and $\nu_\mu \to \nu_\mu$ survival probabilities. We have examined their origin by studying the interrelations of all the three matter probabilities, $P^m_{\mu e}$, $P^m_{\mu\tau}$, and $P^m_{\mu\mu}$, and identified baseline and energy ranges where they act coherently to give observationally large effects. The effects discussed are strongly sensitive to the sign of Δ_{31}, as is apparent from the plots shown in Fig. 4. It is useful to recall Eq. (15) and emphasize that contrary to what one generally assumes, $\Delta P_{\mu\mu}$ is not necessarily negative, i.e. $P^m_{\mu\mu}$ is not always less than or equal to $P^v_{\mu\mu}$. This would be true if large matter effects resided only in $P^m_{\mu e}$, since $\Delta P_{\mu e}$ is positive over the relevant range of energies and baselines. However, as shown earlier, matter effects can not only lead to a substantial enhancement of $P^m_{\mu e}$, but can also cause an appreciable drop or rise in $P^m_{\mu\tau}$, i.e. $\Delta P_{\mu\tau}$ can be significant. Depending on the extent of this, $P^m_{\mu\mu}$ *may be larger or smaller than* $P^v_{\mu\mu}$. In this section, we focus on the detection of matter effects in muon and antimuon survival rates in atmospheric neutrinos.

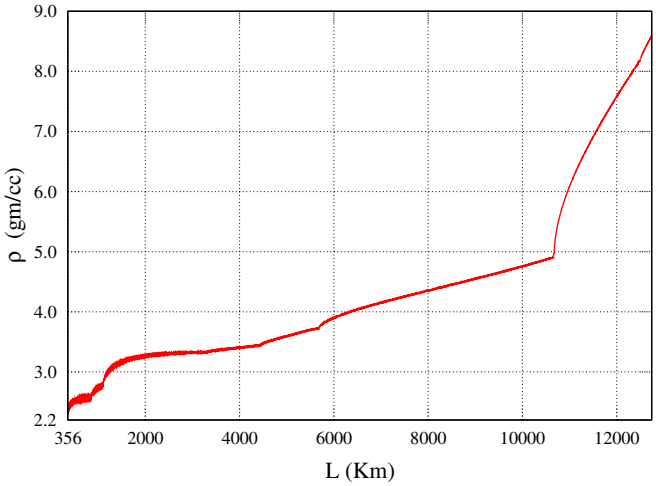

FIG. 13 (color online). The average density ρ for each baseline L, obtained from the PREM density profile, plotted vs L.

Atmospheric neutrinos, while not a controlled source in the sense of the beam experiments described above, offer a compensating advantage: a very broad L/E band extending about 5 orders of magnitude (1 to 10^5 Km/GeV, with neutrino energies, $E_\nu \sim 1$ GeV and above, L from a few Km to about 12 500 Km). The longer baseline lengths allow matter effects to develop and offer possibilities for determination of the mass hierarchy using a detector capable of identifying muon charge. Other physics possibilities with a charge discriminating detector using either atmospheric neutrinos or a neutrino beam as source have been discussed in [38,43,75–77].

Prior to giving the results of our calculations, we briefly describe some of the inputs we have used. The prototype for our calculations is a 100 kT iron detector, with detection and charge discrimination capability for muons provided by a magnetic field of about 1.2 Tesla. Sensitive elements are assumed to be glass spark resistive plate chambers (RPC). We have assumed a (modest) 50% efficiency of the detector for muon detection. This incorporates the kinematic cuts as well as the detection efficiency. The L/E resolution will depend on event kinematics and on muon track detection capabilities.[10] In the calculations presented here, we have used the Bartol [78] atmospheric flux and set a muon detection threshold of 2 GeV. These specifications have been culled from the MONOLITH [79] and INO [80] proposals and hence are realistic to the best of our knowledge. The main systematic errors in this experiment are those that arise in the determination of the energy and the direction (and hence path length) of the neutrino in the initial state. As is true in all neutrino experiments using extra terrestrial sources, the statistical errors are expected to dominate the systematic errors. So,

[10]For our study, we do not use any resolution function. For the most part in what follows, we draw our conclusions based on event rates summed over fairly large ranges in L and/or E.

TABLE II. Number of μ^+ events in matter and in vacuum in restricted bins of E and L for $\Delta_{31} = 0.002$ eV^2 and $\sin^2 2\theta_{13} = 0.1$, $\sin^2 2\theta_{23} = 1.0$.

E (GeV) ⇒ L (Km) ⇓	2–3 N_{mat}, N_{vac}	3–5 N_{mat}, N_{vac}	5–7 N_{mat}, N_{vac}	7–10 N_{mat}, N_{vac}	2–10 N_{mat}, N_{vac}
2000–4000	99, 102	37, 41	11, 12	23, 23	170, 178
4000–6000	55, 59	92, 93	17, 19	3, 3	167, 174
6000–8000	71, 71	47, 48	45, 45	10, 12	173, 176
8000–9700	49, 49	47, 48	27, 25	22, 23	145, 145
9700–10 500	25, 26	20, 21	6, 5	12, 13	63, 65
10 500–12 500	60, 58	54, 55	10, 11	27, 26	151, 150
2000–12 500	359, 365	297, 306	116, 117	97, 100	869, 888

TABLE III. Number of μ^- events in matter and in vacuum in restricted bins of E and L for $\Delta_{31} = 0.002$ eV^2 and $\sin^2 2\theta_{13} = 0.1$, $\sin^2 2\theta_{23} = 1.0$ (see text for details).

E (GeV) ⇒ L (Km) ⇓	2–3 N_{mat}, N_{vac}	3–5 N_{mat}, N_{vac}	5–7 N_{mat}, N_{vac}	7–10 N_{mat}, N_{vac}	2–10 N_{mat}, N_{vac}
2000–4000	229, 233	99, 93	31, 28	55, 53	414, 407
4000–6000	134, 139	191, 215	42, 45	10, 8	377, 407
6000–8000	168, 169	115, 113	**81**, **109**	**21**, **30**	385, 421
8000–9700	120, 118	129, 115	**59**, **63**	**43**, **59**	351, 356
9700–10 500	63, 62	39, 51	24, 13	29, 32	155, 158
10500–12 500	136, 138	118, 138	29, 28	70, 69	353, 373
2000–12 500	850, 859	691, 725	266, 287	228, 251	2035, 2122

in this discussion, we have not taken systematic errors into account.

In order to demonstrate the important qualitative features of our results, we have selectively provided both tables as well as plots of event rates versus L and L/E for positive Δ_{31}. Atmospheric neutrinos offer the advantage of being able to appropriately select ranges in L and E from a large spectrum of L and E values.

An approximate feel for where significant matter effects are likely to show up in muon survival rates can be obtained using our earlier discussion in Secs. II A, II B, and II C, especially that which leads to Eqs. (6), (7), (10), and (16). In particular, the resonance condition [Eq. (6)] gives the following constraint on the product of density and energy:

$$\rho E_{res} = 1.315 \times 10^4 \Delta_{31} \cos 2\theta_{13} \text{ GeV gm}/cc. \quad (26)$$

From Eq. (26), using the value $\Delta_{31} = 0.002$ eV^2 and approximating to the case of a constant average density ρ for any given baseline, one obtains the expression[11]

$$\rho E_{res} \simeq 25 \text{ GeV gm}/cc. \quad (27)$$

In Fig. 13, we plot the average density, ρ as a function of the path length, L for the earth. A rough measure of E_{res} for any given baseline may thus be obtained using this plot and Eq. (27). This is also useful in understanding the broad features of the tables representing our actual calculations and in selecting baseline and energy ranges for closer scrutiny, even though the constant density approximation fails once baselines are very long.

We now proceed with the discussion of our event rate calculations which, as stated earlier, have been performed by solving the full three flavor neutrino propagation equation using PREM [65] density profile of the earth. We have scanned the energy range 2–10 GeV[12] and the L range of 2000–12 500 Km for evidence of matter effects. We have assumed $\Delta_{21} = 8.3 \times 10^{-5}$ eV^2, $\sin^2\theta_{12} = 0.27$ [17], $\delta_{CP} = 0$, and an exposure of 1000 kT-yr for the tables and all plots. Note that for baselines >10 500 Km, passage is through the core of the Earth [81].

In Table II, we show the μ^+ event rates in matter and in vacuum for various energy and baseline bins. As expected, matter effects are *negligible* for antimuons if Δ_{31} is positive.

[11]Note that the resonance condition is not very sensitive to the value of θ_{13}, since the dependence is through a cosine. However, it does depend on what value of Δ_{31} we use. For example, for $\Delta_{31} = 0.002$ eV^2, $\rho E_{res} = 26.3 \times \cos 2\theta_{13}$, which gives $\rho E_{res} = 24.96$ for $\sin^2 2\theta_{13} = 0.1$ and $\rho E_{res} = 26.18$ for $\sin^2 2\theta_{13} = 0.01$. However, for $\Delta_{31} = 0.0015$ eV^2, $\rho E_{res} = 19.7 \times \cos 2\theta_{13}$, giving $\rho E_{res} = 18.7$ for $\sin^2 2\theta_{13} = 0.1$ and $\rho E_{res} = 19.6$ for $\sin^2 2\theta_{13} = 0.01$.

[12]Higher values of energies are also possible, but the falling flux factor considerably diminishes the event rates. Therefore, we take E up to 10 GeV only.

Table III shows the atmospheric event rates for the same bin choices, but for muons. We note that while there are visible differences between matter and vacuum rates, they are not always significantly large. A careful *selection of energy ranges and baselines* is necessary to extract a statistically significant signal. Our plots below reflect these selections. In particular, in Table III, a $\sim 4\sigma$ signal for matter effects can be extracted from the energy bins 5–10 GeV and the L bins 6000–9700 Km (shown in bold text in the table), as discussed below. Consolidating the event rates over large bins in energy and baseline will lead to a dilution, or possibly a washout of the signal, as is evident from this table. For example, the right-most vertical column shows the energy integrated events for the range 2–10 GeV and the last row lists the events integrated over the 2000–12 500 Km baseline range. In both cases, one notes a *dilution* of the signal for matter effects. We also note that for neutrinos passing through the core [81], the difference between the matter and vacuum rates is not appreciable except in the energy range 3–5 GeV for these values of parameters[13] (Table III, sixth row). These effects may be looked for in neutrino factory experiments.

In Fig. 14 we show event rates for muons and antimuons versus L for the baseline and energy bins mentioned above (L = 6000–9700 Km, E = 5–10 GeV). We have assumed $\Delta_{31} = 0.002\text{eV}^2$ and $\sin^2 2\theta_{13} = 0.1$ for this plot. The effect is large for this choice of energies and baselines because it is a combination of the two effects visible in the bottom panels of Fig. 4. The fall in $P^m_{\mu\mu}$ at 9700 Km between 6–15 GeV (which persists over a range of baselines) obtains a large contribution from $P^m_{\mu\tau}$ while the effect shown at 7000 Km arises primarily due to $P^m_{\mu e}$. Both work to lower the muon survival rate below its vacuum value. In contrast to an expected vacuum oscillation rate of 261 events, one expects 204 events in matter if the sign of Δ_{31} is positive.

That we have indeed chosen the bins for which matter effects and sensitivity to the mass hierarchy are maximum, can be demonstrated by a computation of the sensitivity with which the expectation for matter effects with normal hierarchy (NH) differs from that for inverted hierarchy (IH) or for vacuum oscillations. To find the sensitivity, we define

$$\sigma_{\text{NH}-\text{other}} = \frac{|\text{N}_{\text{NH}} - \text{N}_{\text{other}}|}{\sqrt{\text{N}_{\text{NH}}}}, \tag{28}$$

[13]Varying $\sin^2\theta_{23}$ and keeping $\sin^2 2\theta_{13}$ fixed does not change the muon event rates significantly. For instance, for $\sin^2\theta_{23} = 0.6$ and $\sin^2 2\theta_{13} = 0.1$, we get 116 events in matter as compared to 139 events in vacuum in the energy bin E = 3–5 GeV and baseline range L = 10 500–12 500 Km. However, as expected, decreased values of θ_{13} do diminish the statistical significance of the signal. For $\sin^2\theta_{23} = 0.4$ and $\sin^2 2\theta_{13} = 0.05$, we get 132 events in matter while in vacuum we get 140 events in the energy bin E = 3–5 GeV and baseline range L = 10 500–12 500 Km.

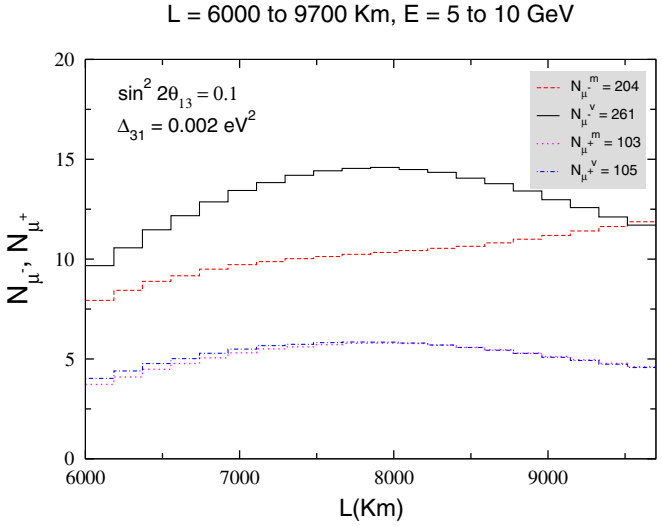

FIG. 14 (color online). Atmospheric muon and antimuon events plotted against L for energy range of 5 to 10 GeV and baselines between 6000 to 9700 Km. The numbers in the legend correspond to the integrated number of muon and antimuon events for the restricted range of L and E in matter and in vacuum for a given value of $\sin^2 2\theta_{13}$.

where $\text{N}_{\text{other}} = \text{N}_{\text{IH}}$ when computing the sensitivity to mass hierarchy $\sigma_{\text{NH}-\text{IH}}$ and $\text{N}_{\text{other}} = \text{N}_{\text{vac}}$ for the sensitivity to matter effects $\sigma_{\text{NH}-\text{vac}}$. We split the 24 bins in Table III into two sets, with fixed values of parameters $\Delta_{31} = 0.002$ eV^2, $\sin^2 2\theta_{23} = 1.0$, $\sin^2 2\theta_{23} = 0.1$. The 4 highlighted bins form one set and the other 20 bins form the second. The sensitivities are calculated using Eq. (28), where the number of events is taken to be the sum of events over each of the sets, thus assuming each set to form a single bin. Now since the number of μ^- events in vacuum will be nearly equal to the number in matter with inverted hierarchy, a signal for matter effect is equivalent to a signal for the mass hierarchy when using only μ^- events. This is brought out in Table IV, where $\sigma_{\text{NH}-\text{IH}}$ is seen to be close to $\sigma_{\text{NH}-\text{vac}}$. Note that this property is specific to a charge discriminating detector. Hence in the subsequent discussion, we describe the values of $\sigma_{\text{NH}-\text{vac}}$ only as a measure of sensitivity to matter effects as well as to the mass hierarchy, when working with only μ^- events.

TABLE IV. Number of μ^- events in vacuum and in matter (normal hierarchy and inverted hierarchy) and corresponding values of σ sensitivity computed by comparing NH-vacuum and NH-IH for 3 different values of $\sin^2 2\theta_{13}$ for the 4 highlighted bins in the E and L range E = 5–10 GeV, L = 6000–9700 Km in Table III. $\Delta_{31} = 0.002$ eV^2 and $\sin^2 2\theta_{23} = 1.0$.

$\sin^2 2\theta_{13}$	N_{vac}	$\text{N}^{\text{NH}}_{\text{mat}}$	$\text{N}^{\text{IH}}_{\text{mat}}$	$\sigma_{\text{NH}-\text{vac}}$	$\sigma_{\text{NH}-\text{IH}}$
0.05	260	227	264	2.2σ	2.5σ
0.1	261	204	262	4.0σ	4.1σ
0.2	263	163	261	7.8σ	7.7σ

TABLE V. Number of μ^- and μ^+ events in vacuum and in matter (normal hierarchy and inverted hierarchy) and corresponding values of NH-vacuum and NH-IH σ sensitivity computed by considering the quantity $(N_{\mu^-} - N_{\mu^+})$ as an observable, for the same values of θ_{13} and E and L ranges as in Table IV. $\Delta_{31} = 0.002$ eV^2 and $\sin^2 2\theta_{23} = 1.0$. This depicts the gain in NH-IH sensitivity if the μ^- as well as μ^+ events are taken into account and the difference is taken to be the observable.

$\sin^2 2\theta_{13}$	$N_{\mu^-}^{vac}$	$N_{\mu^-}^{NH}$	$N_{\mu^-}^{IH}$	$N_{\mu^+}^{vac}$	$N_{\mu^+}^{NH}$	$N_{\mu^+}^{IH}$	σ_{NH-vac}	σ_{NH-IH}
0.05	260	227	264	106	104	94	1.7σ	2.6σ
0.1	261	204	262	105	104	85	3.2σ	4.4σ
0.2	263	163	261	105	102	70	6.0σ	8.0σ

For the sum of μ^- events in the 4 highlighted bins, a large value of $\sigma_{NH-vac} = 4.0\sigma$ is obtained, as seen in the second row of Table IV for the standard value $\sin^2 2\theta_{13} = 0.1$. For the 20 nonhighlighted bins, the corresponding values of event numbers are $N_{vac} = 1860$ and $N_{NH} = 1831$, giving a small $\sigma_{NH-vac} = 0.7\sigma$. If the sum of events of all 24 bins is taken, $N_{vac} = 2121$ and $N_{NH} = 2035$, corresponding to a signal of $\sigma_{NH-vac} = 1.9\sigma$. Thus the 4 highlighted bins give a 4σ signal for matter effect, which also indicates their sensitivity to the mass hierarchy. The above values are for $\sin^2 2\theta_{13} = 0.1$. Table IV also gives the values of NH-vacuum and NH-IH sensitivity for the 4 highlighted bins for two other values of θ_{13}.

In calculating the sensitivities shown in Tables IV and V, we have assumed that the neutrino mass-squared differences and mixing angles will be measured with good precision. Hence no marginalization over these parameters was done in calculating the sensitivities. The ability of a detector to rule out the wrong hierarchy hypothesis, however, does depend on the precision with which the neutrino parameters were measured at that point. Lower precision leads to reduced sensitivity.

Summing over the four highlighted bins in Table III leads to integrating over large ranges in energy and in path length. Hence the detector resolution is not crucial in determining the number of events and the sensitivity. However, the sensitivity is likely to be better if the detector has good energy and path length resolution. The dependence of the sensitivity on detector resolution is currently under study [82].

Figure 15, for the same energy/baseline ranges and parameter values shows the event distributions for muons and antimuons versus L/E.

For a charge discriminating detector, the data for the number of μ^+ events would also be available separately. If the number of μ^+ events is taken into account and the quantity $(N_{\mu^-} - N_{\mu^+})$ is considered as an observable, then the sigma sensitivity is defined as follows:

$$\sigma_{NH-IH} = \frac{(N_{\mu^-}^{NH} - N_{\mu^+}^{NH}) - (N_{\mu^-}^{IH} - N_{\mu^+}^{IH})}{\sqrt{(N_{\mu^-}^{NH} + N_{\mu^+}^{NH})}}. \quad (29)$$

Using this, the NH-IH sensitivity is seen to improve in comparison to the sensitivity obtained using only μ^- events, as seen by comparing Table V with Table IV. However, the NH-vacuum sensitivity suffers a decrease by this method.

The above assumes that the cosmic ray fluxes will be well measured in ten years' time and the atmospheric neutrino fluxes can be predicted with much smaller errors than currently available. If the uncertainty in atmospheric

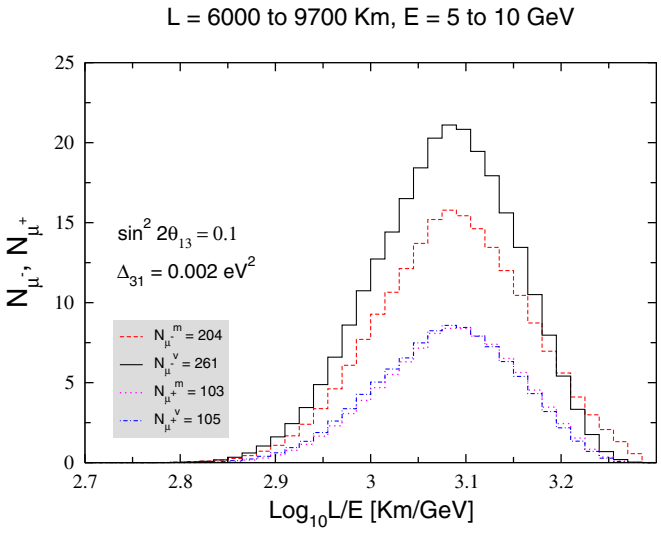

FIG. 15 (color online). The total event rate for muons and antimuons in matter and in vacuum plotted against $\mathrm{Log}_{10}(L/E)$ for the restricted choice of L and E range (see Fig. 14). The numbers in the legend correspond to the integrated number of muon and antimuon events for the restricted range of L and E in matter and in vacuum for a given value of $\sin^2 2\theta_{13}$.

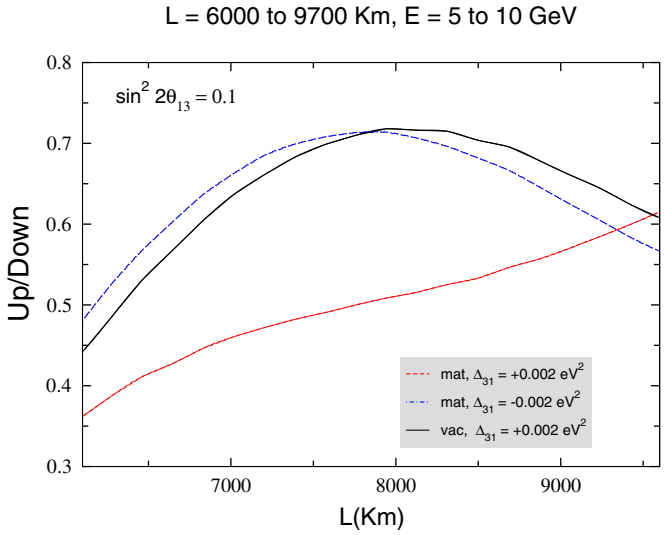

FIG. 16 (color online). Ratio of atmospheric upward and downward going muon (μ^-) events plotted against L for energy range of 5 to 10 GeV and baselines between 6000 to 9700 Km.

TABLE VI. Number of μ^- events in vacuum and in matter (normal hierarchy), number of Down (unoscillated) μ^- events and values of NH-vacuum σ sensitivity computed using ratio of Up/Down events for the same values of θ_{13} and E and L ranges as in Table IV. $\Delta_{31} = 0.002$ eV^2 and $\sin^2 2\theta_{23} = 1.0$.

$\sin^2 2\theta_{13}$	N_{vac}	N^{NH}_{mat}	N_{Down}	σ_{NH-vac}
0.05	260	227	410	1.8σ
0.1	261	204	410	3.3σ
0.2	263	163	410	6.6σ

neutrino flux prediction remains high, then one can use Up/Down event ratios to cancel the normalization uncertainty of the flux predictions. Since the atmospheric neutrino fluxes depend only on the modulus of the cosine of the zenith angle, the muon event rates expected in case of no oscillations can be directly obtained from the experiment, by measuring the rates of downward going muons, binned according to the same energy and the same value of $|\cos\theta|$. Thus the downward going neutrinos provide the necessary information on unoscillated fluxes. Figure 16 shows the Up/Down muon event ratio versus L for L = 6000–9700 Km, E = 5–10 GeV in vacuum and in matter for both signs of Δ_{31}. For this range of energies and baselines, the downward event rates are calculated to be 410 for muons and 164 for antimuons (same in matter and in vacuum). As mentioned earlier, the upward event rate for muons is 204 in matter and 261 in vacuum. For matter oscillations, this gives Up/Down $= 0.50 \pm 0.04$, which differs from the corresponding ratio of 0.64 for vacuum oscillations by $\sim 3.5\sigma$. Table VI lists the values of NH-vacuum sensitivity using the ratio of Up/Down events for the E and L ranges discussed earlier, for three different values of θ_{13}.

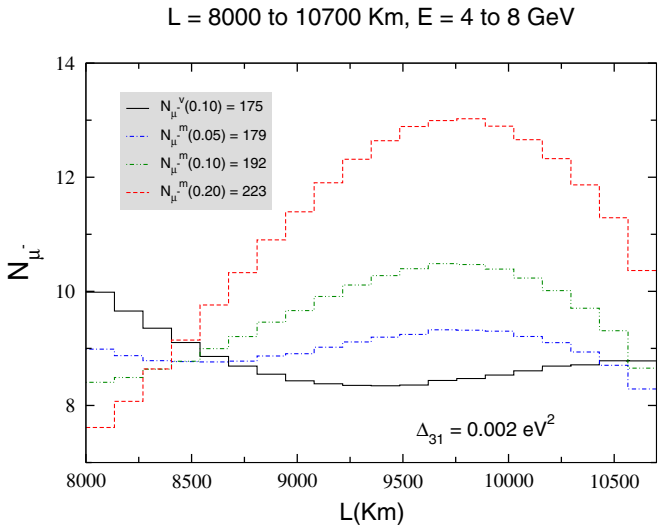

FIG. 17 (color online). Atmospheric muon events plotted against L for energy range of 4 to 8 GeV and baselines between 8000 to 10 700 Km. The numbers in the legend correspond to the integrated number of muon events for the restricted range of L and E in matter and in vacuum for various values of $\sin^2 2\theta_{13}$ (in parenthesis).

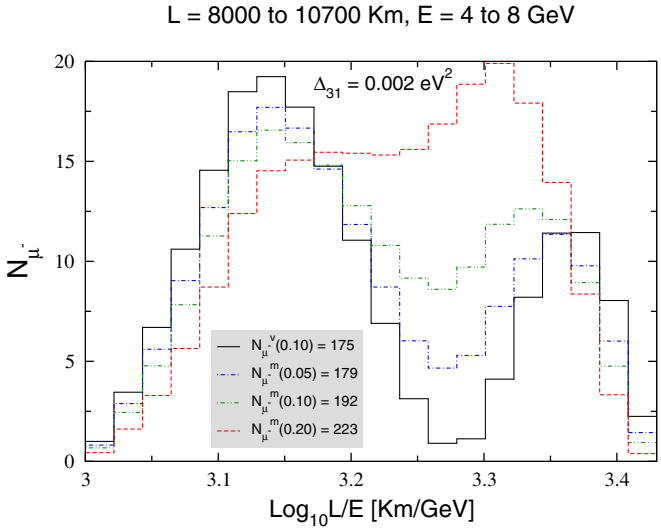

FIG. 18 (color online). The total event rate for muons in matter and in vacuum plotted against Log_{10}(L/E) for the restricted choice of L and E range (see Fig. 17). The numbers in the legend correspond to the integrated number of muon events for the restricted range of L and E in matter and in vacuum for various values of $\sin^2 2\theta_{13}$ (in parenthesis).

As an example of how the muon survival rate can *rise* above the expected vacuum value, we show in Fig. 17 the muon event rate for the baseline range of 8000–10 700 Km and the energy range of 4–8 GeV. The solid curve is the vacuum event rate for $\sin^2 2\theta_{13} = 0.1$, while the three others are the muon survival rates incorporating matter effects for values of $\sin^2 2\theta_{13} = 0.05$, 0.1 and 0.2, respectively.[14] The curves exhibit the rise above the vacuum survival rate visible in the energy range 4–7 GeV in the bottom panel of Fig. 4(a). In addition, the curves demonstrate the sensitivity to θ_{13} which is exhibited in the probability plot given in Fig. 6(b) in the energy range 4–7 GeV. For values of $\sin^2 2\theta_{13}$ close to the present CHOOZ bound, a $>3\sigma$ signal for matter effect is visible in Fig. 17. A similar θ_{13} sensitivity cum event rate plot is also given in Fig. 18 with the muon rate now plotted versus L/E. Here it is seen that N_{μ^-} is particularly sensitive to θ_{13} in the range 3.21–3.34 of Log_{10}(L/E). The value for vacuum oscillations is 23 and it rises to 43 when matter effects are included, even for as small a value as $\sin^2 2\theta_{13} = 0.05$. Treating this Log_{10}(L/E) range as a single bin, $\sigma_{NH-vac} = 3.0$ for $\sin^2 2\theta_{13} = 0.05$, indicating a large signal for matter effect in this bin. Table VII gives the values of σ_{NH-vac} for this Log_{10}(L/E) bin for three different values of θ_{13}, and Table VIII gives the corresponding values of the sensitivity

[14]Note that the vacuum curve will not change appreciably with a change in θ_{13}, so it serves as the reference plot for vacuum.

TABLE VII. Number of μ^- events in vacuum and in matter (normal hierarchy) and corresponding values of NH-vacuum σ sensitivity for 3 different values of $\sin^2 2\theta_{13}$ for the $\mathrm{Log}_{10}(\mathrm{L/E})$ range 3.21–3.34 shown in Fig. 18 (E and L restricted between E = 4–8 GeV, L = 8000–10700 Km). $\Delta_{31} = 0.002$ eV^2 and $\sin^2 2\theta_{23} = 1.0$.

$\sin^2 2\theta_{13}$	N_{vac}	N^{NH}_{mat}	σ_{NH-vac}
0.05	23	43	3.0σ
0.1	23	63	5.0σ
0.2	24	104	7.8σ

TABLE VIII. Number of μ^- events in vacuum and in matter (normal hierarchy), number of Down (unoscillated) μ^- events and values of NH-vacuum σ sensitivity computed using ratio of Up/Down events for the same values of θ_{13} and $\mathrm{Log}_{10}(\mathrm{L/E})$ range as in Table VII. $\Delta_{31} = 0.002$ eV^2 and $\sin^2 2\theta_{23} = 1.0$.

$\sin^2 2\theta_{13}$	N_{vac}	N^{NH}_{mat}	N_{Down}	σ_{NH-vac}
0.05	23	43	156	2.7σ
0.1	23	63	156	4.3σ
0.2	24	104	156	6.1σ

using the Up/Down event ratios. This effect may be looked for provided the L/E resolution is sufficient to observe it. *We note that a significant rise of the muon survival rate in matter over its vacuum values is a signal of the size of the matter effect in* $P_{\mu\tau}$ *overcoming that due to* $P_{\mu e}$, *in spite of the fact that the latter is close to resonance values* [Fig. 4(a), in the energy range 4–7 GeV].

Further demonstration of the sensitivity to the sign of Δ_{31} and of the effects discussed in this paper can be gleaned from plots of the ratio of muon to antimuon event rates $[N_{\mu^-}/N_{\mu^+}]$ [43]. In Fig. 19(a) we show this ratio for the baseline range 6000–9700 Km and the energy range 5–20 GeV. The dominant effect here is due to the reduction in $P^m_{\mu\mu}$ stemming from a large enhancement of $P^m_{\mu e}$, [as evident in the probability plots for 7000 Km in Fig. 4(b) above] and this is clearly visible in the event rates. Comparing the curves for positive and negative Δ_{31}, we see that the peak to peak difference between them is about 90%.

Selecting different (lower) ranges in both baselines and energy, we show the rate ratio for 4000–9000 Km and 3–10 GeV in Fig. 19(b). As evident from the discussion of the previous section, the $P^m_{\mu\tau}$ effects develop after 8000 Km for the most part, hence this choice is primarily suited to demonstrate the effect of $P^m_{\mu e}$ on $P^m_{\mu\mu}$. The influence of $P^m_{\mu\tau}$ is, however, visible at the higher baselines, as it draws the $\Delta_{31} > 0$ curve close to the vacuum curve because, as discussed above, the $P^m_{\mu e}$ and $P^m_{\mu\tau}$ effects work in the opposite direction in this region. The dip-peak separation for the curves for $\Delta_{31} > 0$ and $\Delta_{31} < 0$ is about 60% in this case.

Finally, in an attempt to show an example of a baseline/energy range where both effects, i.e. the effect where $P^m_{\mu\tau}$ plays a major role by raising the rate ratio above its vacuum value, and the effect where the resonant rise in $P^m_{\mu e}$ domi-

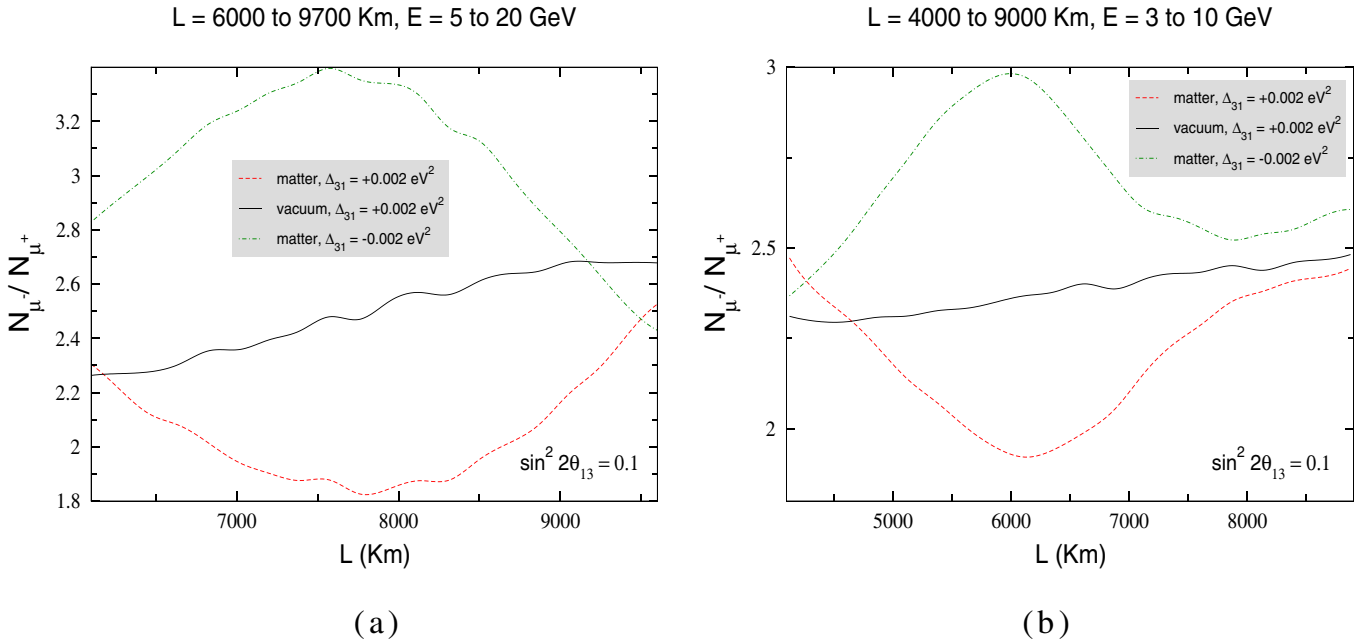

FIG. 19 (color online). (a) and (b) depict the ratio of atmospheric muon and antimuon events plotted against L for two different wide energy ranges (5–20 GeV and 3–10 GeV) and two baseline ranges (6000–9700 Km and 4000–9000 Km, respectively).

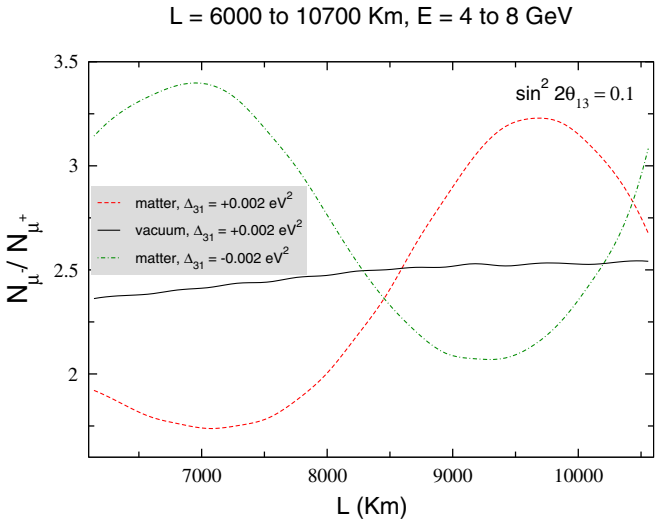

FIG. 20 (color online). Ratio of atmospheric muon and antimuon events plotted against L for energy range of 4 to 8 GeV and baselines between 6000 to 10 700 Km. For the restricted energy range considered here, the ratio for the case of matter oscillations with NH is greater than that of the vacuum ratio, when L is greater than 9000 Km. This is because of the increase of $P_{\mu\mu}$ caused by the sharp fall in $P_{\mu\tau}$.

nates over $P^m_{\mu\tau}$ to bring about a decrease in N_{μ^-}/N_{μ^+} compared to its value in vacuum, we choose the baseline range 6000–10 700 Km and the energy range 4–8 GeV (Fig. 20). For $\Delta_{31} > 0$, the dip in the ratio is maximum around 7000 Km and originates from the drop in the probability visible in the bottom panel of Fig. 4(b), while the rise above the vacuum curve, which is maximum around 9700 Km, is a manifestation of *the increase in* $P_{\mu\mu}$ *consequent to the large decrease in* $P_{\mu\tau}$ *occurring in the range 4–8 GeV*, shown in Figs. 4(a) and 6(b).

IV. CONCLUSIONS

To conclude, we summarize the salient points of our study:

(i) In addition to $P_{\mu e}$, interesting and appreciable matter effects can arise in $P_{\mu\tau}$ at baselines >7000 Km. These can synergistically combine to give correspondingly large effects in $P^m_{\mu\mu}$. As a result, observably large signals may appear in a charge discriminating detector capable of measuring muon survival rates, providing a useful handle on the sign of Δ_{31}.

(ii) The resonance amplified matter effects in $P^m_{\mu\tau}$ may be observable in future experimental facilities with intense ν_μ beams and detectors capable of τ identification.

(iii) We find that both $P^m_{\mu\tau}$ and $P^m_{\mu\mu}$ are sensitive to θ_{13}. We have identified baselines and energies where the matter effects are amplified by the resonance and the sensitivity to θ_{13} is high. We also have studied the θ_{23} dependence of $P^m_{\mu\tau}$ and $P^m_{\mu\mu}$.

(iv) We have performed a detailed study of parameter degeneracies at very long baselines, using numerical results with a realistic Earth density profile. We find that for these baselines and at energies for which the criterion $1.27\Delta_{31}L/E = n\pi/2$ is satisfied, $P^m_{\mu e}$ is largely free of the degeneracies which could obscure measurements of θ_{13} and sign(Δ_{31}). The $(\delta_{CP}, \theta_{13})$ degeneracy is lifted for $P^m_{\mu\tau}$ and $P^m_{\mu\mu}$ also. The sign(Δ_{31}) degeneracy vanishes for $P^m_{\mu\tau}$ at such baselines and energies, but can be present in $P^m_{\mu\mu}$ for some specific values of θ_{13} and δ_{CP}. We also note that the determination of θ_{13} from $P^m_{\mu\tau}$ does not suffer from the $(\theta_{23}, \pi/2 - \theta_{23})$ degeneracy, $P^m_{\mu\tau}$ being a function of $\sin 2\theta_{23}$. Further, for the baselines and energies relevant for us this degeneracy disappears from $P^m_{\mu\mu}$ and $P^m_{\mu e}$ as well.

(v) In the second part of the paper we perform detailed calculations of muon survival rates for atmospheric neutrinos, using a 100 kT charge discriminating iron calorimeter as prototype. Our choice here is guided by our motivation to explore whether it is possible to realistically determine the sign of Δ_{31} in an atmospheric neutrino experiment, over a time scale shorter than that anticipated for neutrino factories.

(vi) While atmospheric neutrinos make available a wide range of baselines and energies, we find that in order to detect matter effects using total event rates, a careful screening and selection of L and E is necessary to overcome the lack of a high intensity beam. We use our earlier discussion of matter effects in $P^m_{\mu e}$, $P^m_{\mu\tau}$, and $P^m_{\mu\mu}$ as a guide to identify fairly broad L and E ranges where the sensitivity to the sign of Δ_{31} is significantly large. As an example, $P^m_{\mu\tau}$ and $P^m_{\mu e}$ combine constructively in the range 5–10 GeV and 6000–9700 Km to yield a potentially large signal ($\sim 4\sigma$) for matter effect for $\Delta_{31} > 0$ ($\sim 3.5\sigma$ for the Up/Down ratio). We also identify regions where an appreciable sensitivity to θ_{13} exists. For a large mass iron calorimeter type detector, a 3σ discrimination is seen in the 3.2–3.5 range of $\mathrm{Log}_{10}(L/E)$ for $\sin^2 2\theta_{13}$ as low as 0.05.

(vii) We have discussed the possibility of detection of matter effects and the sign of Δ_{31} using a charge discriminating iron calorimeter. Although these effects appear only for ν_μ for Δ_{31} positive (and only for $\bar{\nu}_\mu$ for Δ_{31} negative), it may also be possible to look for them using high statistics megaton water Cerenkov detectors like Hyper-Kamiokande in Japan and UNO in the U.S. [27,34]. These effects may also be searched for in the accumulated SK data.

ACKNOWLEDGMENTS

We would like to thank S. Choubey, M. V. N. Murthy, and P. Roy for suggestions and discussions. We also acknowledge useful communications from M. Lindner, E. Lisi, S. Palomares-Ruiz, S. Petcov, A. Takamura, and W. Winter. S. G. acknowledges support from the Alexander von Humboldt Foundation.

[1] Y. Fukuda *et al.* (Kamiokande Collaboration), Phys. Lett. B **335**, 237 (1994).
[2] Y. Fukuda *et al.* (Super-Kamiokande Collaboration), Phys. Rev. Lett. **81**, 1562 (1998).
[3] Y. Fukuda *et al.* (Super-Kamiokande Collaboration), Phys. Rev. Lett. **82**, 2644 (1999).
[4] E. Kearns, *Proceedings of the XXIst International Conference on Neutrino Physics and Astrophysics (Neutrino-2004), Paris*, see http://neutrino2004.in2p3.fr/.
[5] M. Ambrosio *et al.* (MACRO Collaboration), Phys. Lett. B **566**, 35 (2003); M. Ambrosio *et al.* (MACRO Collaboration), Eur. Phys. J. C **36**, 323 (2004).
[6] W. W. M. Allison *et al.* (SOUDAN-2 Collaboration), Phys. Lett. B **449**, 137 (1999).
[7] R. Becker-Szendy *et al.*, *Proceedings of the 16th International Conference on Neutrino Physics and Astrophysics (Neutrino-94)* [Nucl. Phys. B, Proc. Suppl. 38, 331 (1995)].
[8] M. H. Ahn *et al.* (K2K Collaboration), Phys. Rev. Lett. **90**, 041801 (2003); T. Nakaya, *Proceedings of the XXIst International Conference on Neutrino Physics and Astrophysics (Neutrino-2004), Paris* [Nucl. Phys. B, Proc. Suppl. 143, 96 (2005)].
[9] C. Cattadori, *Proceedings of the XXIst International Conference on Neutrino Physics and Astrophysics (Neutrino-2004), Paris* [Nucl. Phys. B, Proc. Suppl. 143, 3 (2005)].
[10] B. T. Cleveland *et al.*, Astrophys. J. **496**, 505 (1998).
[11] J. N. Abdurashitov *et al.* (SAGE Collaboration), J. Exp. Theor. Phys. **95**, 181 (2002); V. Gavrin, *Proceedings of the VIIth International Conference on Topics in Astroparticle and Underground Physics (TAUP03), Seattle, 2003*, see http://www.int.washington.edu/talks/WorkShops/TAUP03/Parallel/.
[12] W. Hampel *et al.* (GALLEX Collaboration), Phys. Lett. B **447**, 127 (1999).
[13] M. Altmann *et al.* (GNO Collaboration), Phys. Lett. B **490**, 16 (2000); E. Bellotti, *Proceedings of the VIIth International Conference on Topics in Astroparticle and Underground Physics (TAUP03), Seattle, 2003*, see http://www.int.washington.edu/talks/WorkShops/TAUP03/Parallel/.
[14] S. Fukuda *et al.* (Super-Kamiokande Collaboration), Phys. Lett. B **539**, 179 (2002).
[15] Q. R. Ahmad *et al.* (SNO Collaboration), Phys. Rev. Lett. **87**, 071301 (2001); **89**, 011301 (2002); **89**, 011302 (2002).
[16] S. N. Ahmed *et al.* (SNO Collaboration), Phys. Rev. Lett. **92**, 181301 (2004).
[17] K. Eguchi *et al.* (KAMLAND Collaboration), Phys. Rev. Lett. **90**, 021802 (2003); T. Araki *et al.* (KAMLAND Collaboration), Phys. Rev. Lett. **94**, 081801 (2005).
[18] L. Wolfenstein, Phys. Rev. D **17**, 2369 (1978); S. P. Mikheev and A. Y. Smirnov, Sov. J. Nucl. Phys. **42**, 913 (1985) [Yad. Fiz. **42**, 1441 (1985)].
[19] S. Goswami, *Proceedings of the XXIst International Conference on Neutrino Physics and Astrophysics (Neutrino-2004), Paris* [Nucl. Phys. B, Proc. Suppl. 143, 121 (2005)].
[20] J. N. Bahcall, M. C. Gonzalez-Garcia, and C. Pena-Garay, J. High Energy Phys. 08 (2004) 016.
[21] M. Maltoni, T. Schwetz, M. A. Tortola, and J. W. F. Valle, New J. Phys. **6**, 122 (2004).
[22] M. C. Gonzalez-Garcia, *Proceedings of the Nobel Symposium 2004 on Neutrino Physics, Sweden*, see http://www.physics.kth.se/nobel2004/program.html, hep-ph/0410030.
[23] P. Huber, M. Lindner, M. Rolinec, T. Schwetz, and W. Winter, Phys. Rev. D **70**, 073014 (2004); Nucl. Phys. B, Proc. Suppl. **145**, 190 (2005).
[24] E. Ables *et al.* (MINOS Collaboration), Fermilab Report No. P875, 1995; P. Adamson *et al.* (MINOS Collaboration), MINOS Technical Design Report No. Nu-MI-L-337, 1998; see http://www-numi.fnal.gov/; A. Marchionni *et al.* (MINOS Collaboration), in *Proceedings of the 7th International Workshop on Neutrino Factories and Superbeams (NuFact05), Frascati* (Fermilab Report No. FERMILAB-CONF-05-429-AD-E); M. Thomson, *Proceedings of the XXIst International Conference on Neutrino Physics and Astrophysics (Neutrino-2004), Paris* [Nucl. Phys. B, Proc. Suppl. 143, 249 (2005)]; P. Shanahan, Eur. Phys. J. C **33**, s834 (2004).
[25] P. Aprili *et al.* (ICARUS Collaboration), CERN, Report No. CERN-SPSC-2002-027; A. Bueno, *Proceedings of the XXIst International Conference on Neutrino Physics and Astrophysics (Neutrino-2004), Paris* [Nucl. Phys. B, Proc. Suppl. 143, 262 (2005)]; J. Lagoda, *Proceedings of The 4th International Conference on Non-accelerator New Physics (NANP 2003), Dubna*, see http://nanp.ru/2003/program.html.
[26] D. Duchesneau (OPERA Collaboration), eConf C0209101, TH09 (2002) [Nucl. Phys. B, Proc. Suppl. **123**, 279 (2003)].D. Autiero, *Proceedings of the XXIst International Conference on Neutrino Physics and Astrophysics (Neutrino-2004), Paris*, see http://neutrino2004.in2p3.fr/; M. Dracos, *Proceedings of The 4th International Conference on Non-accelerator New Physics (NANP 2003), Dubna*, see http://nanp.ru/2003/program.html.

[27] Y. Hayato, *Proceedings of the XXIst International Conference on Neutrino Physics and Astrophysics (Neutrino-2004), Paris* [Nucl. Phys. B, Proc. Suppl. 143, 269 (2005)]; Y. Itow *et al.*, hep-ex/0106019; see http://neutrino.kek.jp/jhfnu/.

[28] D. S. Ayres *et al.* (NOVA Collaboration), Fermilab, Report No. FERMILAB-PROPOSAL-0929, hep-ex/0503053; also see http://www-nova.fnal.gov/; A. Weber, Eur. Phys. J. C **33**, s843 (2004); M. Messier, *Proceedings of the XXIst International Conference on Neutrino Physics and Astrophysics (Neutrino-2004), Paris*, see http://neutrino2004.in2p3.fr/.

[29] E. A. K. Abouzaid *et al.*, http://www-library.lbl.gov/docs/LBNL/565/99/PDF/LBNL-56599.pdf; K. Anderson *et al.*, hep-ex/0402041.

[30] F. Suekane (KASKA Collaboration), *Proceedings of the 5th Workshop on Neutrino Oscillations and Their Origin (NOON2004), Tokyo, Japan, 2004*, see http://www-sk.icrr.u-tokyo.ac.jp/noon2004/, hep-ex/0407016; F. Suekane, K. Inoue, T. Araki, and K. Jongok, *Proceedings of the 4th Workshop on Neutrino Oscillations and Their Origin (NOON2003), Kanazawa, Japan, 2003*, hep-ex/0306029.

[31] M. H. Shaevitz and J. M. Link, hep-ex/0306031; also see http://theta13.lbl.gov/ and http://braidwood.uchicago.edu/; L. Oberauer, *Proceedings of the XXIst International Conference on Neutrino Physics and Astrophysics (Neutrino-2004), Paris* [Nucl. Phys. B, Proc. Suppl. 143, 277 (2005)].

[32] M. Apollonio *et al.* (CHOOZ Collaboration), Phys. Lett. B **466**, 415 (1999); M. Apollonio *et al.* (CHOOZ Collaboration), Eur. Phys. J. C **27**, 331 (2003).

[33] T. Lasserre, *Proceedings of the 5th Workshop on Neutrino Oscillations and Their Origin (NOON2004), Tokyo*, see http://www-sk.icrr.u-tokyo.ac.jp/noon2004/; see also http://doublechooz.in2p3.fr/.

[34] C. K. Jung, in *Proceedings of the International Workshop on Next Generation Nucleon Decay and Neutrino Detector (NNN99), Stony Brook*, edited by M. V. Diwan and C. K. Jung, AIP Conf. Proc. No. 533 (AIP, New York, 2000); also see http://ale.physics.sunysb.edu/uno/publications.shtml/; K. Nakamura, *Proceedings of the Conference on Neutrinos and Implications for Physics Beyond the Standard Model, C. N. Yang Institute for Theoretical Physics, SUNY, Stony Brook, 2002*, see http://insti.physics.sunysb.edu/itp/conf/neutrino/talks/nakamura.pdf.

[35] J. Bernabeu, S. Palomares-Ruiz, and S. T. Petcov, Nucl. Phys. **B669**, 255 (2003).

[36] T. Kajita, *Proceedings of The 5th Workshop on Neutrino Oscillations and Their Origin (NOON2004), Tokyo*, see http://www-sk.icrr.u-tokyo.ac.jp/noon2004/; H. Gallagher, *Proceedings of the XXIst International Conference on Neutrino Physics and Astrophysics (Neutrino-2004), Paris* [Nucl. Phys. B, Proc. Suppl. 143, 79 (2005)].

[37] A. Yu. Smirnov, *Proceedings of The 5th Workshop on Neutrino Oscillations and Their Origin, (NOON2004), Tokyo*, see http://www-sk.icrr.u-tokyo.ac.jp/noon2004/.

[38] C. Albright *et al.*, hep-ex/0008064; M. Apollonio *et al.*, hep-ph/0210192 and references therein; C. Albright *et al.* (Neutrino Factory/Muon Collider Collaboration), physics/0411123.

[39] R. Gandhi, P. Ghoshal, S. Goswami, P. Mehta, and S. Uma Sankar, Phys. Rev. Lett. **94**, 051801 (2005).

[40] M. C. Banuls, G. Barenboim, and J. Bernabeu, Phys. Lett. B **513**, 391 (2001).

[41] J. Bernabeu and S. Palomares-Ruiz, *Proceedings of the International Europhysics Conference on High-Energy Physics (HEP2001), Budapest, 2001*, hep-ph/0112002.

[42] T. Tabarelli de Fatis, Eur. Phys. J. C **24**, 43 (2002).

[43] S. Palomares-Ruiz and S. T. Petcov, Nucl. Phys. **B712**, 392 (2005).

[44] D. Indumathi and M. V. N. Murthy, Phys. Rev. D **71**, 013001 (2005).

[45] R. Gandhi, P. Mehta, and S. Uma Sankar, a note prepared for solar and atmospheric working group of the American Physical Society, Report No. HRI-P-04-10-001.

[46] M. Diwan *et al.*, hep-ex/0211001; M. V. Diwan *et al.*, Phys. Rev. D **68**, 012002 (2003).

[47] A. Rubbia, Nucl. Phys. B, Proc. Suppl. **147**, 103 (2005).

[48] V. D. Barger, K. Whisnant, S. Pakvasa, and R. J. N. Phillips, Phys. Rev. D **22**, 2718 (1980).

[49] C. W. Kim, W. K. Sze, and S. Nussinov, Phys. Rev. D **35**, 4014 (1987).

[50] S. M. Bilenky, Fiz. Elem. Chastits At. Yadra **18**, 449 (1987); S. M. Bilenky and S. T. Petcov, Rev. Mod. Phys. **59**, 671 (1987); **61**, 169(E) (1989).

[51] H. W. Zaglauer and K. H. Schwarzer, Z. Phys. C **40**, 273 (1988).

[52] J. Pantaleone, Phys. Lett. B **292**, 201 (1992).

[53] G. L. Fogli, E. Lisi, D. Montanino, and G. Scioscia, Phys. Rev. D **55**, 4385 (1997).

[54] T. Ohlsson and H. Snellman, J. Math. Phys. (N.Y.) **41**, 2768 (2000); **42**, 2345(E) (2001); Phys. Lett. B **474**, 153 (2000) **480**, 419(E) (2000).

[55] Z. z. Xing, Phys. Lett. B **487**, 327 (2000).

[56] M. Freund, M. Lindner, S. T. Petcov, and A. Romanino, Nucl. Phys. **B578**, 27 (2000); M. Freund, P. Huber, and M. Lindner, Nucl. Phys. **B585**, 105 (2000); M. Freund, M. Lindner, S. T. Petcov, and A. Romanino, Nucl. Instrum. Methods Phys. Res., Sect. A **451**, 18 (2000); M. Freund, Phys. Rev. D **64**, 053003 (2001).

[57] T. Ohlsson, Phys. Scr. **T93**, 18 (2001).

[58] T. Ota and J. Sato, Phys. Rev. D **63**, 093004 (2001).

[59] See e.g. I. Mocioiu and R. Shrock, Phys. Rev. D **62**, 053017 (2000); I. Mocioiu and R. Shrock, J. High Energy Phys. 11 (2001) 050.

[60] V. D. Barger, S. Geer, R. Raja, and K. Whisnant, Phys. Rev. D **62**, 013004 (2000); Phys. Lett. B **485**, 379 (2000).

[61] K. Kimura, A. Takamura, and H. Yokomakura, Phys. Lett. B **537**, 86 (2002); Phys. Rev. D **66**, 073005 (2002); Phys. Lett. B **544**, 286 (2002).

[62] B. Brahmachari, S. Choubey, and P. Roy, Nucl. Phys. **B671**, 483 (2003).

[63] P. F. Harrison, W. G. Scott, and T. J. Weiler, Phys. Lett. B **565**, 159 (2003).

[64] E. K. Akhmedov, R. Johansson, M. Lindner, T. Ohlsson, and T. Schwetz, J. High Energy Phys. 04 (2004) 078.

[65] A. M. Dziewonski and D. L. Anderson, Phys. Earth Planet Inter. **25**, 297 (1981); see http://solid_earth.ou.edu/prem.html. We use the parametrization given in R. Gandhi, C. Quigg, M. H. Reno, and I. Sarcevic, Astropart. Phys. **5**, 81 (1996).

[66] See the first reference in [56].
[67] R. Gandhi, P. Ghoshal, S. Goswami, P. Mehta, and S. Uma Sankar (work in progress).
[68] V. Barger, D. Marfatia, and K. Whisnant, Phys. Rev. D **65**, 073023 (2002); Phys. Rev. D **66**, 053007 (2002); Phys. Lett. B **560**, 75 (2003).
[69] P. Huber and W. Winter, Phys. Rev. D **68**, 037301 (2003).
[70] M. Lindner, Nucl. Phys. B, Proc. Suppl. **118**, 199 (2003); M. Lindner, Springer Tracts Mod. Phys. **190**, 209 (2003).
[71] H. Minakata and H. Nunokawa, J. High Energy Phys. 10 (2001) 001; T. Kajita, H. Minakata, and H. Nunokawa, Phys. Lett. B **528**, 245 (2002); H. Minakata, H. Nunokawa, and S. J. Parke, Phys. Rev. D **66**, 093012 (2002).
[72] J. Burguet-Castell, M. B. Gavela, J. J. Gomez Cadenas, P. Hernandez, and O. Mena, Nucl. Phys. **B608**, 301 (2001); M. Aoki, K. Hagiwara, and N. Okamura, Phys. Lett. B **606**, 371 (2005); O. Yasuda, New J. Phys. **6**, 83 (2004).
[73] A. Cervera, A. Donini, M. B. Gavela, J. J. Gomez Cadenas, P. Hernandez, O. Mena, and S. Rigolin, Nucl. Phys. **B579**, 17 (2000); **B593**, 731(E) (2001).
[74] A. Donini, D. Meloni, and P. Migliozzi, Nucl. Phys. **B646**, 321 (2002).
[75] Tests of CPT using atmospheric neutrinos in such a detector have been discussed in A. Datta, R. Gandhi, P. Mehta, and S. Uma Sankar, Phys. Lett. B **597**, 356 (2004).
[76] D. Choudhury and A. Datta, J. High Energy Phys. 07 (2005) 058.
[77] S. Choubey and P. Roy, Phys. Rev. Lett. **93**, 021 803 (2004).
[78] V. Agrawal, T. K. Gaisser, P. Lipari, and T. Stanev, Phys. Rev. D **53**, 1314 (1996).
[79] N. Y. Agafonova *et al.* (MONOLITH Collaboration), Report No. LNGS-P26-2000; http://castore.mi.infn.it/~monolith/.
[80] See http://www.imsc.res.in/~ino and working group reports and talks therein.
[81] Core effects in atmospheric neutrinos have been discussed in S. T. Petcov, Phys. Lett. B **434**, 321 (1998); E. K. Akhmedov, A. Dighe, P. Lipari, and A. Y. Smirnov, Nucl. Phys. **B542**, 3 (1999); M. Chizhov, M. Maris, and S. T. Petcov, hep-ph/9810501; M. V. Chizhov and S. T. Petcov, Phys. Rev. D **63**, 073003 (2001); J. Bernabeu, S. Palomares-Ruiz, A. Perez, and S. T. Petcov, Phys. Lett. B **531**, 90 (2002).
[82] R. Gandhi, P. Ghoshal, S. Goswami, P. Mehta, and S. Uma Sankar (work in progress).